The Astrophysical Journal, 1000:111 (25pp), 2026 March 20 https://doi.org/10.3847/1538-4357/ae3b25
© 2026. The Author(s). Published by the American Astronomical Society.
OPEN ACCESS

# Galaxies in the Epoch of Reionization Are All Bark and No Bite—Plenty of Ionizing Photons, Low Escape Fractions

Casey Papovich[1,2], Justin W. Cole[1,2,26], Weida Hu[1,2], Steven L. Finkelstein[3], Lu Shen[1,2], Pablo Arrabal Haro[4,27], Ricardo O. Amorín[5], Bren E. Backhaus[6], Micaela B. Bagley[3,4], Rachana Bhatawdekar[7], Antonello Calabrò[8], Adam C. Carnall[9], Nikko J. Cleri[10,11,12], Emanuele Daddi[13], Mark Dickinson[14], Norman A. Grogin[15], Benne W. Holwerda[16], Anne E. Jaskot[17], Anton M. Koekemoer[15], Mario Llerena[8], Ray A. Lucas[15], Sara Mascia[18], Fabio Pacucci[19,20], Laura Pentericci[8], Pablo G. Pérez-González[21], Nor Pirzkal[22], Srinivasan Raghunathan[23], Lise-Marie Seillé[24], Rachel S. Somerville[25], and L. Y. Aaron Yung[15]

[1] Department of Physics and Astronomy, Texas A&M University, College Station, TX 77843-4242, USA; papovich@tamu.edu
[2] George P. and Cynthia Woods Mitchell Institute for Fundamental Physics and Astronomy, Texas A&M University, College Station, TX 77843-4242, USA
[3] Department of Astronomy, The University of Texas at Austin, Austin, TX 78712, USA
[4] Astrophysics Science Division, NASA Goddard Space Flight Center, 8800 Greenbelt Rd, Greenbelt, MD 20771, USA
[5] Instituto de Astrofísica de Andalucía (CSIC), Apartado 3004, 18080 Granada, Spain
[6] Department of Physics and Astronomy, University of Kansas, Lawrence, KS 66045, USA
[7] European Space Agency (ESA), European Space Astronomy Centre (ESAC), Camino Bajo del Castillo s/n, 28692, Villanueva de la Cañada, Madrid, Spain
[8] INAF–Osservatorio Astronomico di Roma, via di Frascati 33, 00078, Monte Porzio Catone, Rome, Italy
[9] Institute for Astronomy, University of Edinburgh, Royal Observatory, Edinburgh, EH9 3HJ, UK
[10] Department of Astronomy and Astrophysics, The Pennsylvania State University, University Park, PA 16802, USA
[11] Institute for Computational and Data Sciences, The Pennsylvania State University, University Park, PA 16802, USA
[12] Institute for Gravitation and the Cosmos, The Pennsylvania State University, University Park, PA 16802, USA
[13] Université Paris-Saclay, Université Paris Cité, CEA, CNRS, AIM, 91191, Gif-sur-Yvette, France
[14] NSF's National Optical-Infrared Astronomy Research Laboratory, 950 N. Cherry Avenue, Tucson, AZ 85719, USA
[15] Space Telescope Science Institute, 3700 San Martin Drive, Baltimore, MD 21218, USA
[16] Department of Physics, University of Louisville, Louisville, 40292 KY, USA
[17] Department of Physics and Astronomy, Williams College, Williamstown, MA 01267, USA
[18] Institute of Science and Technology Austria (ISTA), Am Campus 1, A-3400 Klosterneuburg, Austria
[19] Center for Astrophysics | Harvard & Smithsonian, 60 Garden St, Cambridge, MA 02138, USA
[20] Black Hole Initiative, Harvard University, 20 Garden St, Cambridge, MA 02138, USA
[21] Centro de Astrobiología (CAB/CSIC-INTA), Ctra. de Ajalvir km 4, Torrejón de Ardoz, E-28850, Madrid, Spain
[22] ESA/AURA Space Telescope Science Institute, USA
[23] Center for AstroPhysical Surveys, National Center for Supercomputing Applications, Urbana, IL 61801, USA
[24] Aix Marseille Univ, CNRS, CNES, LAM, Marseille, France
[25] Center for Computational Astrophysics, Flatiron Institute, 162 5th Avenue, New York, NY 10010, USA
*Received 2025 May 13; revised 2026 January 12; accepted 2026 January 16; published 2026 March 16*

## Abstract

Early results from JWST suggest that Epoch of Reionization (EoR) galaxies produce copious ionizing photons, which, if they escape efficiently, could cause reionization to occur too early. We study this problem using JWST imaging and prism spectroscopy for 412 galaxies at $4.5 < z < 9.0$. We fit these data simultaneously with stellar population and nebular emission models that include a parameter for the fraction of ionizing photons that escape the galaxy, $f_{\rm esc}$. We find that the ionization production efficiency, $\xi_{\rm ion} = Q(H_0)/L_{\rm UV}$, increases with redshift and decreasing UV luminosity, but shows significant scatter, $\sigma(\log \xi_{\rm ion}|z, M_{\rm UV}) \simeq 0.3$ dex. The inferred escape fractions averaged over the population are low, ranging from $\langle f_{\rm esc}\rangle \simeq 2.6\% \pm 1.4\%$ at $6 < z < 9$ to $6.5\% \pm 2.2\%$ at $4.5 < z < 6$, with weak or no indication of evolution with redshift. This implies that in our models most of the ionizing photons need to be absorbed to account for the nebular emission. We compute the impact of our results on reionization, including the distributions for $\xi_{\rm ion}$ and $f_{\rm esc}$, and the evolution and uncertainty of the UV luminosity function. Considering galaxies brighter than $M_{\rm UV} < -16$ mag would produce an intergalactic medium hydrogen-ionized fraction of $x_e = 0.5$ at $5.3 < z < 5.8$, possibly too late compared to constraints from from quasi-stellar object (QSO) sight lines. Including fainter galaxies, $M_{\rm UV} < -14$ mag, we obtain $x_e = 0.5$ at $6.0 < z < 8.1$, fully consistent with QSO and cosmic microwave background data. This implies that EoR galaxies produce plenty of ionizing photons, but that these do not efficiently escape. This may be a result of high gas column densities combined with burstier star formation histories, which limit the time massive stars are able to clear channels through the gas for ionizing photons to escape.

*Unified Astronomy Thesaurus concepts:* Stellar populations (1622); Emission line galaxies (459); Reionization (1383); Galaxy evolution (594); James Webb Space Telescope (2291)

[26] NASA FINESST Fellow.
[27] NASA Postdoctoral Fellow.

Original content from this work may be used under the terms of the Creative Commons Attribution 4.0 licence. Any further distribution of this work must maintain attribution to the author(s) and the title of the work, journal citation and DOI.

## 1. Introduction

JWST has transformed our ability to characterize the nature of galaxies at redshifts as high as $z \sim 14$ (e.g., P. Arrabal Haro et al. 2023a; A. J. Bunker et al. 2023; S. Carniani et al. 2024; V. Kokorev et al. 2025). From analyses of JWST data, galaxies

at $z > 7$ appear to be dominated by younger stellar populations (e.g., C. Papovich et al. 2023), with stronger nebular emission (A. Calabrò et al. 2024; S. Mascia et al. 2024; C. Simmonds et al. 2024a, 2024b; R. Endsley et al. 2025; A. Pahl et al. 2025), and evidence of more bursty star formation histories (J. W. Cole et al. 2025; R. Endsley et al. 2025; J. A. A. Trussler et al. 2025) compared to lower-redshift galaxies (e.g., J. W. Cole et al. 2025; L. Shen et al. 2025).

The properties of galaxies at $z > 6$ are crucially important because this period corresponds to the Epoch of Reionization (EoR) of the intergalactic medium (IGM). Constraints from the polarization of the cosmic microwave background (CMB) show that the ionized fraction of the IGM rises from nil at the Epoch of Recombination, $z \approx 1100$, to $x_e = 0.5$ by $z = 8.4$ (Planck Collaboration et al. 2020).[28] This can be combined with observations of the optical depth of ionizing radiation from quasi-stellar objects (QSOs) to show that reionization had effectively "ended" by $z \sim 5$–$6$ when the ionized fraction was $x_e \gtrsim 0.9$ (e.g., I. D. McGreer et al. 2015; B. Greig et al. 2017; G. D. Becker et al. 2019; W. Hu et al. 2019; C. A. Mason et al. 2019; F. Wang et al. 2020; L. R. Whitler et al. 2020; M. Nakane et al. 2024).

Galaxies during the first billion years appear to be the most likely cause of this reionization (see B. E. Robertson et al. 2023). Observations from JWST have already shown evidence that galaxies at $z \gtrsim 7$ have sufficient ionizing radiation to complete reionization by this time (C. Simmonds et al. 2024a, 2024b). The primary quantity of interest is the so-called ionizing production efficiency, $\xi_{\rm ion}$, defined as the ratio of the production rate of photons with energies >13.6 eV, $Q(H_0)$, in units of $s^{-1}$, to the luminosity density at 1500 Å, $L_{\rm UV}$, in units of erg $s^{-1}$ $Hz^{-1}$ (C. Leitherer & T. M. Heckman 1995). Analysis of JWST data shows that $\xi_{\rm ion}$ spans a wide range, from as low $\log \xi_{\rm ion} \simeq 24.5$ to as high as $\log \xi_{\rm ion} \simeq 25 - 26$ (e.g., G. Prieto-Lyon et al. 2023; H. Atek et al. 2024; C. Simmonds et al. 2024a, 2024b; R. Begley et al. 2025; M. J. Hayes et al. 2025; M. Llerena et al. 2025; A. Pahl et al. 2025), possibly exceeding the canonical value, $\log \xi_{\rm ion} = 25.2$, expected for young stellar populations and observed for galaxies at $z \sim 2$ (B. E. Robertson et al. 2015; I. Shivaei et al. 2018). That is, EoR galaxies appear to produce sufficient ionizing radiation for reionization to proceed.

However, we lack a good understanding of how much of this radiation escapes into the IGM. This is measured by the escape fraction, $f_{\rm esc}$, which is the relative amount of photons with energies greater than the ionization energy of hydrogen (also referred to as Lyman-continuum radiation, LyC, at wavelengths <912 Å). Theoretical constraints predict that the escape fraction is low for EoR galaxies as the column density of gas that fuels star formation is very large (e.g., A. Ferrara & A. Loeb 2013; H. Xu et al. 2016). The key is how efficiently feedback from star formation can clear channels through the gas, allowing LyC photons to escape (T. Kimm & R. Cen 2014). Current predictions suggest that EoR galaxies with masses similar to those detected with JWST will have lower escape fractions, with $f_{\rm esc} \sim 1\%$–$15\%$ (X. Ma et al. 2015; H. Xu et al. 2016; A. Ferrara et al. 2019; J. Y. C. Yeh et al. 2023; I. Kostyuk et al. 2025), although some simulations argue for an increase in $f_{\rm esc}$ with increasing redshift (e.g., J. Rosdahl et al. 2022; M. Trebitsch et al. 2022). As these galaxies are expected to drive reionization (J. S. W. Lewis et al. 2020), it is of paramount importance to constrain $f_{\rm esc}$ in galaxies at these redshifts.

Measuring the escape fraction is challenging. At low redshifts, it must be observed from space. Some results for starburst and extreme-emission-line galaxies show high values, $f_{\rm esc} = 6\%$–$35\%$ (Y. I. Izotov et al. 2016, 2021), but the value for an individual galaxy appears to depend strongly on the geometry (Y. Choi et al. 2020). Work from the Low-Redshift Lyman Continuum Survey (LzLCS; S. R. Flury et al. 2022a) has showed that, for $z \sim 0.3$ galaxies, $f_{\rm esc}$ generally increases with decreasing galaxy luminosity, increasing ionization parameter (often parameterized by the [O III]/[O II] ratio or by the Balmer emission equivalent width, EW), decreasing UV spectral slope ($\beta_{\rm UV}$), and decreasing dust attenuation (e.g., S. R. Flury et al. 2022b). It is not known if these correlations are causal or related to underlying processes. A. E. Jaskot et al. (2024) showed that $f_{\rm esc}$ has less scatter when using a multivariate analysis, implying a more complex relationship between $f_{\rm esc}$ and galaxy properties. Nevertheless, the application of the LzLCS relations to EoR galaxies predicts the latter should have relatively high escape fractions, in excess of 10% (J. Chisholm et al. 2022; F. Cullen et al. 2023; S. Mascia et al. 2024).

At higher redshifts the escape fraction can only be detected directly for galaxies at $z \lesssim 4$, as at higher redshifts the density of H I absorbers in the IGM becomes too large to detect any escaping LyC photons (e.g., A. K. Inoue et al. 2014). Measurements of $f_{\rm esc}$ from galaxies at $1 < z < 3.5$ find low *average* values, $\langle f_{\rm esc} \rangle \leqslant 7\%$ (B. Siana et al. 2010; K. Boutsia et al. 2011; D. B. Nestor et al. 2013; A. Grazian et al. 2017; J. Matthee et al. 2017; C. C. Steidel et al. 2018; A. J. Pahl et al. 2021, 2023; R. Begley et al. 2022; A. Saxena et al. 2022; I. Jung et al. 2024; X. Wang et al. 2025), in agreement with constraints on the global escape fraction from the H I photoionization rate in the IGM inferred from the Ly$\alpha$ forest, which require $f_{\rm esc} \simeq 1\%$–$2\%$ (F. Haardt & P. Madau 2012; V. Khaire & R. Srianand 2015). However, $f_{\rm esc}$ may vary significantly, where individual reports span 20%–100% (see, e.g., Y. I. Izotov et al. 2021; A. Saxena et al. 2022). Moreover, the average $f_{\rm esc}$ appears to be higher for galaxies with stronger emission lines (e.g., C. C. Steidel et al. 2018; A. J. Pahl et al. 2021), which may be more typical of EoR galaxies. Therefore, it remains unclear what, if anything, we can infer about the nature of $f_{\rm esc}$ for EoR galaxies using these results.

Combining all of these results poses a potential problem. Pre-JWST studies (B. E. Robertson et al. 2015; S. L. Finkelstein et al. 2019; L. Y. A. Yung et al. 2020a) found that a wide range of $f_{\rm esc}$ ($f_{\rm esc} \simeq 3\%$–$30\%$) could be capable of producing reionization. JWST observations now show that EoR galaxies produce higher quantities of ionizing photons (see above), which, when combined with high $f_{\rm esc}$ values, would cause reionization to occur too early (J. B. Muñoz et al. 2024). These details depend crucially on the distributions of $\xi_{\rm ion}$ and $f_{\rm esc}$, their dependence on the UV luminosity, and on the evolution of the UV luminosity function (UVLF). For the latter, we have reached a consensus, based on deep-field studies from the Hubble Space Telescope (HST) and JWST , that the UVLF at $7 < z < 10$ follows a power law down to galaxies as faint as $M_{\rm UV} < -15$ (S. L. Finkelstein & M. B. Bagley 2022; G. C. K. Leung et al. 2023; P. G. Pérez-González et al. 2023;

[28] The Planck Collaboration et al. (2020) analysis also suggests a nonzero optical depth of CMB photons scattering off free electrons at $z \approx 15$, which implies ionization of the IGM had begun by this epoch.

N. J. Adams et al. 2024; C. T. Donnan et al. 2024). Further, studies from lensed galaxies provide evidence that this extends to at least $M_{\rm UV} < -13$ (R. C. Livermore et al. 2017; R. Bhatawdekar et al. 2019; H. Atek et al. 2024), notably fainter than the LMC and SMC (M. Maucherat-Joubert et al. 1980). J. B. Muñoz et al. (2024) showed that, given this evolution of the UVLF, if EoR galaxies have high $\xi_{\rm ion}$, *and* high $f_{\rm esc}$, then the global emissivity, $\dot{n}/({\rm s}^{-1}\ {\rm Mpc}^{-3})$, is potentially too high, creating a "photon budget crisis" (see also P. Ocvirk et al. 2021). This stresses the importance of constraining $\xi_{\rm ion}$ and $f_{\rm esc}$ in EoR galaxies.

Here, we study this problem using a new analysis of JWST imaging and spectroscopy from the Cosmic Evolution Early Release Science (CEERS) survey and JWST Advanced Deep Extragalactic survey (JADES), focusing on galaxies at $4.5 < z < 9.0$ with photometry from HST and JWST and spectroscopy from the JWST/NIRSpec PRISM. These data cover the rest-frame region from the rest-frame far-UV (∼1500 Å) through the H$\beta$ (+ [O III]) lines (or to H$\alpha$, depending on the redshift). We model these spectroscopic and imaging data for each galaxy simultaneously, where the strength of the nebular emission is compared to the shape of the rest-UV/optical continuum. With this, we can infer an *indirect* estimate of the escape fraction, as the modeling constrains the number of ionizing photons and the nebular emission constrains the number that do *not* escape. There is precedence for this type of analysis based on observations of H II regions (M. S. Oey & R. C. Kennicutt 1997) and resolved stars in the starburst galaxy NGC 4214 (Y. Choi et al. 2020). In both cases, these studies use observations of the far-UV and nebular emission to constrain the number of LyC photons, and then compare this to the emission in the nebular component. At high redshift, similar analyses have attempted to constrain $f_{\rm esc}$, finding that some galaxies have $f_{\rm esc} = 50\%$–$80\%$ (M. W. Topping et al. 2022). Here, we test the ability of the SED modeling to constrain $f_{\rm esc}$ using both real and simulated galaxies (see Section 4.2 and Appendix B). Applying this to the real data for the $4.5 < z < 9.0$ galaxies, we find that the nebular emission is sufficiently strong to account for nearly all of the produced ionizing photons: the escape fractions are low, typically less than a few percent for most galaxies.

The outline for the paper is as follows. In Section 2, we discuss the CEERS and JADES datasets, and how we selected our sample. In Section 3, we discuss the analysis methods used to model the stellar populations and nebular emission of the galaxies based on their imaging and spectroscopic data. We also discuss the measurements of emission-line fluxes from the spectroscopic data. In Section 4, we discuss the constraints on $\xi_{\rm ion}$ and $f_{\rm esc}$, their distributions as a function of UV luminosity and redshift, and how these constrain $\dot{n}$. In Section 5, we discuss how $\xi_{\rm ion}$ and $f_{\rm esc}$ depend on galaxy properties, and consider the implications of our results for reionization. In Section 6, we present our conclusions.

We adopt a flat cosmology throughout with $\Omega_{m,0} = 0.315$, $H_0 = 67.4\ {\rm km\,s^{-1}\,Mpc^{-1}}$, and $\Omega_{b,0} = 0.0493$ (Planck Collaboration et al. 2020). All magnitudes reported here are in the AB system (J. B. Oke & J. E. Gunn 1983). We use a G. Chabrier (2003) initial mass function (IMF) for relevant quantities. We also frequently drop the units for the ionization production efficiency, $\xi_{\rm ion}$, which are $({\rm s^{-1}\ (erg\ s^{-1}\ Hz^{-1})^{-1}})^{-1}$.

## 2. Data and Sample

For this work, we select galaxies with excellent multi-wavelength coverage from HST and JWST imaging, and spectroscopy from the JWST/NIRSpec PRISM. The prism data are important because they cover the wavelength range 0.8–5.3 $\mu$m contiguously, with a spectral resolution varying from $R \sim 80$ at $\simeq$2.5 $\mu$m to $R \sim 300$ at $\simeq$5 $\mu$m. This provides measurements of the galaxy continua and emission features, which can be modeled to constrain the properties of the stellar populations and nebular gas. However, the prism spectra face additional challenges including the fact that the amount of flux received depends on the galaxy morphology, the location of the galaxy within the Microshutter Array (MSA) slitlet, the wavelength-dependent image quality and spatial resolution. This is a primary reason we combine the prism data with the photometric imaging. Because the imaging provides matched-aperture flux densities over a wide wavelength range, typically 0.6–5 $\mu$m, we can model these simultaneously with the prism data to measure any flux-calibration issues from the data themselves.

### 2.1. CEERS Data

CEERS is a JWST Early Release Survey that provides JWST imaging and spectroscopy of the legacy CANDELS/EGS field (S. L. Finkelstein et al. 2025). CEERS includes NIRCam and MIRI imaging, as described in M. B. Bagley et al. (2023) and G. Yang et al. (2023). We use an updated photometric catalog following a similar procedure as that in S. L. Finkelstein et al. (2024). This includes matched-aperture flux-density measurements from JWST/NIRCam with the F115W, F150W, F200W, F277W, F356W, F410M, and F444W filters, combined with HST imaging from the Advanced Camera for Surveys (ACS) in the F606W and F814W filters, and from the Wide Field Camera 3 (WFC3) IR in the F125W and F160W, with partial coverage from F105W and F140W. All HST data are drawn from the archival observations of these fields, with most coming from CANDELS (N. A. Grogin et al. 2011; A. M. Koekemoer et al. 2011). For 22 of the 114 of the CEERS spectroscopic sources (≈20%), no JWST/NIRCam imaging exists. For these, we use the HST-based catalog of S. L. Finkelstein et al. (2022), which includes the HST imaging above combined with Spitzer/IRAC imaging at 3.6 and 4.5 $\mu$m. We include these objects for completeness, but we have verified that removing them does not affect the results. The CEERS MIRI data include deep imaging in F560W and F770W in two pointings that overlap with NIRCam (G. Yang et al. 2023), and we include those data where they are available following C. Papovich et al. (2023).

We use the JWST/NIRSpec PRISM data for CEERS, with additional NIRSpec PRISM data obtained in the CEERS field from P. Arrabal Haro et al. (2023a). The data-reduction steps are described in P. Arrabal Haro et al. (2023b), and we use the most recent version available (v0.9; P. Arrabal Haro et al. 2026, in preparation) We then use an internal catalog of spectroscopic redshifts from the CEERS team based on the LIne MEasuring library (V. Fernández et al. 2024).

### 2.2. JADES Data

We include published data from JADES (D. J. Eisenstein et al. 2023), which provides JWST/NIRCam imaging and NIRSpec PRISM data for galaxies in the GOODS-N and

GOODS-S fields. Here, we use the photometric catalog from K. N. Hainline et al. (2024), which includes flux-density measurements from JWST/NIRCam, and HST/ACS and WFC3/IR. For GOODS-N, these include imaging from NIRCam using the F090W, F115W, F150W, F182M, F200W, F210M, F277W, F335M, F356W, F410M, and F444W filters, combined with HST imaging from ACS in F435W, F606W, F775W, F814W, and F850LP, and WFC3/IR in F105W, F125W, F140W, and F160W. The GOODS-S catalog includes all the filters used for GOODS-N combined with additional NIRCam medium-band imaging in F430M, F460M, and F480M (C. C. Williams et al. 2023).

The JADES NIRSpec PRISM data provide spectroscopy for ∼4000 galaxies in the GOODS-N and GOODS-S fields (F. D'Eugenio et al. 2025).

### 2.3. Sample Selection

Our goal is to study the ionization conditions, escape fractions, and stellar population parameters in galaxies at redshifts near and into the EoR. To this end, we select galaxies from JADES and CEERS that meet the following criteria: (1) broadband imaging coverage as listed in the photometric catalogs above, (2) NIRSpec PRISM data from the datasets above, and (3) a confirmed spectroscopic redshift placing them at $4.5 < z < 9.0$. For this last step, the lower redshift bound ensures that the NIRSpec PRISM data cover the rest-frame far-UV (∼1500 Å), while the upper redshift bound ensures the data cover the important rest-frame optical strong emission lines, H$\beta$ + [O III] $\lambda\lambda$4959, 5008. The former will be important for constraining the rest-frame UV luminosity, while the latter will be important for constraining the number of ionizing photons, and therefore the ionizing production efficiency and inferred escape fraction.

We select from the JADES catalog (F. D'Eugenio et al. 2025) all galaxies with $4.5 \leqslant z < 9.0$ with a spectroscopic quality flag of "A" or "B." This results in a sample of 129 galaxies in GOODS-N and 183 galaxies in GOODS-S, after removing duplicates (keeping the spectrum with higher signal-to-noise ratio, S/N, following a visual inspection; see F. D'Eugenio et al. 2025). We then remove candidate active galactic nuclei (AGN), either based on X-ray detections (H. Xu et al. 2016; B. Luo et al. 2017) or identified as possible AGN by I. Juodžbalis et al. (2026) or D. D. Kocevski et al. (2025). This reduced the JADES sample to 123 galaxies in GOODS-N and 175 galaxies in GOODS-S. From CEERS, we select galaxies from the internal team release that includes data from all CEERS NIRSpec observations, with redshifts from an automatic line finder (V. Fernández et al. 2024), and visual inspection by multiple CEERS team members. We again remove possible AGN using D. D. Kocevski et al. (2025); no galaxies are detected in the current X-ray coverage of the CEERS field. We identify 114 unique galaxies in CEERS in this redshift range.

Figure 1 shows the redshift distribution of the samples. While JADES provides more spectra overall, their distribution is weighted toward galaxies at the lower-redshift end of our range. The CEERS data fill in the distribution at higher redshifts. This redshift range covers galaxies from the period after reionization ends, $z \gtrsim 5$ (G. D. Becker et al. 2019), through the period when it begins, $z \gtrsim 8$ (Planck Collaboration et al. 2020). Nevertheless, selection effects will remain important as our sample requires the presence of spectroscopic

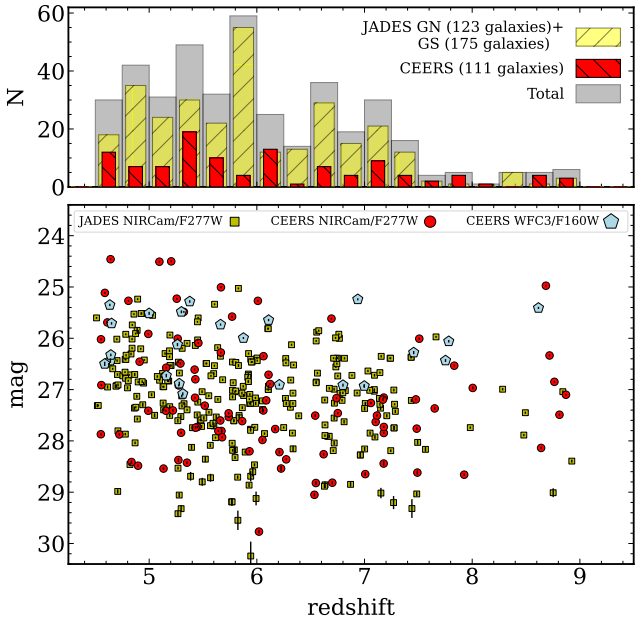


**Figure 1.** Redshift and magnitude distributions of the spectroscopic sources at $4.5 < z < 9.0$ used in this work. The top panel shows histograms of the distribution of sources from JADES GOODS-N (GN) and GOODS-S (GS), CEERS, and the total (the sum of the two), as labeled. JADES includes more galaxies overall, but is weighted toward galaxies at the lower end of our redshift range. The CEERS sample is more evenly spread in redshift, and provides greater coverage at the higher-redshift end of the range. The bottom panel shows the redshift vs. NIRCam F277W magnitude distribution for galaxies in JADES and CEERS. A minority of the CEERS galaxies lack NIRCam imaging; for these, we show the WFC3 F160W magnitude instead.

feature(s) to be included in the sample (i.e., emission lines). For all galaxies in our sample, this includes the presence of the [O III] 4959, 5008 doublet and other lines. Future studies with deeper exposures, primarily using NIRSpec PRISM, will be needed to obtain more complete samples based on redshifts that do not necessarily depend on the presence of emission lines. This will be possible in the future with surveys such as CAPERS (M. Dickinson et al. 2024). We return to the importance of selection effects below in Section 5.

## 3. Analysis

### 3.1. Spectral Energy Distribution Modeling

We fit the spectral energy distributions (SEDs) of the galaxies in our sample using stellar population synthesis models. We model each galaxy using `BAGPIPES` (v1.3.1, A. C. Carnall et al. 2018), a Bayesian SED-fitting code capable of simultaneously fitting multiband photometry and spectroscopy using stellar population synthesis models and nebular emission models generated over a wide range of parameters. The code allows flexibility in the choice of stellar population models, star formation histories, dust attenuation, and nebular emission. It computes posterior probability densities for the model parameters given the data by calculating a likelihood weighted by priors, and samples these posteriors using `nautilus` (J. U. Lange 2023). The newest version of `BAGPIPES` also includes updated `Cloudy` nebular models (v25; C. M. Gunasekera et al. 2025).

We have added several features to `BAGPIPES` for our analysis. First, one of our goals is to determine the constraints on the inferred LyC escape fraction, $f_{\rm esc}$. By default, the current nebular emission models in `BAGPIPES` generated

from Cloudy assume 100% of the incident radiation is absorbed and used to generate the nebular emission (i.e,. $f_{esc} = 0$). Following A. M. Morales et al. (2024), we have added a parameter (nebular:fesc) such that the nebular emission is reduced by a factor of $1 - f_{esc}$. This models the LyC escape as a fraction of sight lines that are "clear" (akin to a covering fraction equal to $(1 - f_{esc})$). As we show, the majority of galaxies favor very low escape fractions of <5%, implying such clear channels are infrequent. In a future work, we plan to explore other types of $f_{esc}$, including cases where the nebulae are truncated or "density bounded" (K. Nakajima & M. Ouchi 2014; A. Plat et al. 2019).

Second, there are several processes that can impact the shape of the UV continuum with respect to the stars. One process is the nebular continuum, produced from free–bound and two-photon emission from the $2s \rightarrow 1s$ transition in hydrogen. These are already included in the BAGPIPES Cloudy models. Another process is increased H I absorption from the IGM or the interstellar medium (ISM) of the host galaxy, both of which can alter the shape of the UV spectra, particularly around Ly$\alpha$. Several studies have measured an increase in the strength of the H I damping wing in galaxies at the EOR (K. E. Heintz et al. 2024; H. Umeda et al. 2024). We have added to BAGPIPES the H I damping wing to allow for this effect, following the formalism of M. Dijkstra (2014). This requires two parameters: IGM:R, the comoving distance to the patch of IGM at the edge of the ionized "bubble" around a galaxy, and IGM:x_HI, the average gas-neutral fraction of the patch of the IGM (see also K. E. Heintz et al. 2024). This allows the models not to rely excessively on the nebular continuum to reproduce the shape of the rest-UV continuum.

Third, through testing we found that modeling of the JWST/NIRSpec data frequently underfits the spectral resolution. BAGPIPES uses a model for the variable spectral resolution of the NIRSpec PRISM, available from the Space Telescope Science Institute (STScI),[29] but this assumes galaxies are unresolved and are centered in the MSA slits. The reality is that the effects of galaxy morphology and location within the slit lead to a type of morphological spectral broadening, similar to that seen in slitless data (R. C. Simons et al. 2023). Indeed, recent updates to the NIRSpec calibration find this effect is wavelength dependent and can be as large as 50%.[30] To compensate, we include a nuisance parameter that multiplies the spectral resolution by a factor with respect to the spectral file (which we refer to as a line-spread facto, LSF). This parameter improves the quality of the fits, particularly in the widths of the nebular emission lines. We allow the galaxy spectra to be broadened by an intrinsic velocity dispersion, $\sigma_v$, though in practice this is much less than the instrument dispersion. We also allow the noise to be scaled by a nuisance parameter, and allow for a multiplicative scaling factor (assumed to be a second-order polynomial) to match the spectral flux to the broadband photometry.

Table 1 lists the parameters, limits, and priors we used with BAGPIPES for the SED fitting. We use the Binary Population and Spectral Synthesis (BPASS, v2.2.1) models from E. R. Stanway & J. J. Eldridge (2018), assuming a Chabrier IMF with an upper stellar mass cutoff of 300 $M_{\odot}$, and including the effects of stellar binaries. This choice is motivated by the fact that high-redshift galaxies appear to require additional ionization from high-mass stars (e.g., H. Katz et al. 2025), and, as we show below, these models reasonably reproduce both the spectral continua and emission-line intensities (consistent with other results; see, e.g., L. M. Seillé et al. 2024). For the star formation history, we employ the parameterization of K. G. Iyer et al. (2019), which uses Gaussian processes to represent the star formation rate (SFR) in different time bins, with a boundary condition that it produces the instantaneous SFR and stellar mass at the moment of observation. We choose three time bins corresponding to when the star formation history has formed 25%, 50%, and 75% of the stellar mass ($t_{25}$, $t_{50}$, and $t_{75}$, respectively). We also tested the use of star formation histories with fixed time bins (e.g., J. Leja et al. 2019). Using bins that sample the time quasi-logarithmically, following R. Begley et al. (2025), we find that this has no net impact on our results. We nevertheless adopt star formation histories parameterized by Gaussian processes (K. G. Iyer et al. 2019) as they provide flexibility in the star formation history to account for bursts and quenching events without setting a prior on the width of the star formation time bins.

We adopt the D. Calzetti (2001) dust attenuation law, which is appropriate for more highly attenuated, blue star-forming galaxies (where for less attenuated galaxies the differences between the Calzetti law and alternatives such as the SMC are small; see B. Salmon et al. 2016). We also assume the stellar continua and nebular emission are attenuated by the same amount (N. A. Reddy et al. 2015), which is appropriate as our galaxies generally have low dust attenuation, with young ages (M. Lecroq et al. 2024), so systematic shifts in the attenuation will have minimal impact on our results (R. L. Sanders et al. 2021; L. Shen et al. 2025). We use the dust attenuation derived from the SED fitting to correct emission-line fluxes and the UV continuum. We opt not to use the Balmer lines, as not all lines are available for all galaxies and the SED fitting incorporates all available information (see also A. P. Vijayan et al. 2025). As we show below (Section 3.4), the $\xi_{ion}$ values derived from dust-corrected H$\alpha$ and H$\beta$ are consistent, which further justifies these choices. For the escape fraction, we adopted a logarithmic prior; that is, one that is linear in $\log f_{esc}$. This choice resulted from our experiments, which show that most galaxies have low $f_{esc}$, and that the logarithmic prior allows us to better sample the posterior at low values of $f_{esc}$. We verified that this choice has no impact on our conclusions.

We then use BAGPIPES to fit these models to the observed photometry and NIRSpec PRISM data for each galaxy. We used the Texas A&M High Performance Research Computing Grace cluster to perform the calculations.[31] Grace is a Dell x86 HPC cluster with 800 48-core compute nodes, each equipped with 384 Gb RAM. Run times for the fit to converge for each galaxy are typically 1–4 hr of CPU time.

Figures 2 and 3 show results from the SED modeling of example galaxies from the CEERS and JADES samples, respectively. These galaxies illustrate the quality of the fits from which we derive results. The galaxies all show strong rest-UV continua with a "break" at rest-frame Ly$\alpha$. Furthermore, all show evidence of rest-optical emission lines, [O III] 5008, and H$\beta$ 4861, and H$\alpha$ 6564 for galaxies with $z < 6.7$.

[29] https://jwst-docs.stsci.edu/files/97979440/97979447/1/1596073265467/jwst_nirspec_prism_disp.fits

[30] https://www.stsci.edu/contents/news/jwst/2025/new-pathloss-corrections-for-nirspec-multi-object-and-fixed-slit-spectroscopy-are-available

[31] Named for Grace Hopper (https://en.wikipedia.org/wiki/Grace_Hopper).

**Table 1**
Parameter Settings for BAGPIPES

| Model Component | Parameter | Prior | Limits |
|---|---|---|---|
| | Redshift, $z$ | $N(\mu = z_{\rm sp}, \sigma = 5\sigma_z)$[a] | $z_{\rm sp} \pm 0.2$ |
| Star formation history (K. G. Iyer et al. 2019): Dense-basis, Gaussian processes | Instantaneous SFR/$M_\odot$ yr$^{-1}$ | $\log_{10}$ | $(10^{-3}, 10^{3})$ |
| | Lookback times to bin $X$, $\{t_X\}$/yr | Dirichlet | $X = \{25, 50, 75\}$ |
| | Stellar mass, $\log(M_*/M_\odot)$ | Uniform | (6, 13) |
| Dust attenuation | Attenuation law | … | D. Calzetti (2001) |
| | Attenuation, $A(V)$/mag | Uniform | (0, 2) |
| Metallicity | $Z/Z_\odot$ | Uniform | (0, 1) |
| Nebular emission | Ionization parameter, $\log U$ | Uniform | (−4, 0) |
| | Escape fraction, $f_{\rm esc}$ | $\log_{10}$ | $(10^{-4}, 1)$ |
| IGM damping wing | Size of bubble, $R$/cMpc | Uniform | (0,150) |
| | Average neutral fraction, $\bar{x}_e$ | Uniform | (0.0, 1.0) |
| NIRSpec specific | Line-spread factor (LSF) | Uniform | (1.0, 6.6) |
| | Velocity dispersion, $\sigma_v$/(km s$^{-1}$) | $\log_{10}$ | (50, 1000) |
| | Noise scaling factor | $\log_{10}$ | (1, 10) |
| Flux-calibration factor applied to spectra: second-order polynomial, $A_0 + A_1\lambda + A_2\lambda^2$ | $A_0$ | $\log_{10}$ | (0.1, 10) |
| | $A_1$ | $N(\mu = 0, \sigma = 0.25)$ | (− 0.5, 0.5) |
| | $A_2$ | $N(\mu = 0, \sigma = 0.25)$ | (− 0.5, 0.5) |

**Note.**
[a] $N(\mu, \sigma)$ corresponds to a Gaussian, "normal" prior described by mean, $\mu$, and variance, $\sigma^2$.

These features are well fit in both the prism data (lower panels in the figures) and in the broadband photometry (upper panels). In some cases, the prism data show evidence of rest-UV emission lines, e.g., C III] 1909 in CEERS MPT ID DDT 28 (in Figure 2).

### 3.2. Measuring $M_{UV}$, $\beta_{UV}$, and $f_{esc}$

For this analysis, we focus on the evolution of the ionizing production efficiency, $\xi_{\rm ion}$, and the LyC escape fraction, $f_{\rm esc}$, as a function of $M_{\rm UV}$. We also consider trends between $f_{\rm esc}$ and the UV spectral slope, $\beta_{\rm UV}$, $f_\lambda \propto \lambda^{\beta_{\rm UV}}$, defined using regions devoid of emission features over rest-frame 1268–2580 Å (D. Calzetti et al. 1994). For the UV spectral slope, we measure this from the NIRSpec data after correcting for the slit-loss flux calibration (see above). For $M_{\rm UV}$ and $f_{\rm esc}$, we derive their constraints for each galaxy from the SED fits. For each galaxy, we take 400 model fits drawn from the posterior. For each model, we measure the 1500 Å rest-frame flux density, $F_{1500}$, using a top-hat filter from 1450–1550 Å, and then calculate the rest-frame UV (1500 Å) absolute magnitude by applying the distance modulus. In practice, we compute $M_{\rm UV}$ twice: once for the dust-corrected spectrum and once without. We use the dust-corrected measurement to estimate $\xi_{\rm ion}$, but we use the observed $M_{\rm UV}$ with no dust correction when we consider the production of ionizing photons based on the galaxy UVLF (in Section 4.3). For each galaxy, we take $M_{\rm UV}$ and $f_{\rm esc}$ as the median of the draws from the posterior, with an uncertainty from the 16th to 84th percentiles. We also derive constraints on other stellar population parameters, such as stellar mass, SFR, and dust attenuation. The latter we use to correct the derived quantities and emission-line fluxes.

### 3.3. Measuring Emission-line Fluxes and Equivalent Widths

We measure emission-line EWs and line fluxes from the NIRSpec PRISM spectra. In principle, we could take the emission-line measurements from the BAGPIPES SED fits directly; however, these models assume a priori knowledge. This includes in particular the chemical abundances, where BAGPIPES scales the metallicity with a solar abundance pattern. As this assumption is still under debate, with several studies arguing for $\alpha$-enrichment in these early galaxies (e.g., A. G. Beverage et al. 2024; M. Park et al. 2025), we opt to measure the emission fluxes directly from the data, using the SED fits as guidance. In Appendix A, we compare the directly measured emission-line fluxes with those predicted from SED modeling. We show that they are in good agreement for the strong optical emission lines ([O III], H$\beta$, and H$\alpha$), but exhibit higher scatter for [O II].

For each galaxy, we correct for dust attenuation and calibration/slit-loss corrections using the results from the SED modeling (see Section 3.1). This factor varies from ∼0.5 to 2.0 at the wavelength of the redshifted H$\beta$ line for each galaxy, with a median (68th to 84th percentile range) of 0.77 (0.60–0.99) for JADES (with no difference seen between GOODS-N and GOODS-N) and 1.52 (0.83–2.62) for CEERS. Applying this factor ensures that the NIRSpec spectra are adjusted in a robust fashion to match the photometry, and corrects for any wavelength-dependent calibration issues. We compared the EWs of the H$\beta$ and [O III] lines measured from the raw spectra with the corrected spectra, and find that they agree to within $<10^{-4}$ dex, with a scatter of $\leqslant$0.04 dex. We then use the SED modeling to provide an estimate of the continuum for each spectrum, excluding the contribution from nebular emission lines. This step is crucial for measuring accurate EWs, and for measuring accurate Balmer emission-line fluxes when nonnegligible stellar absorption is present.

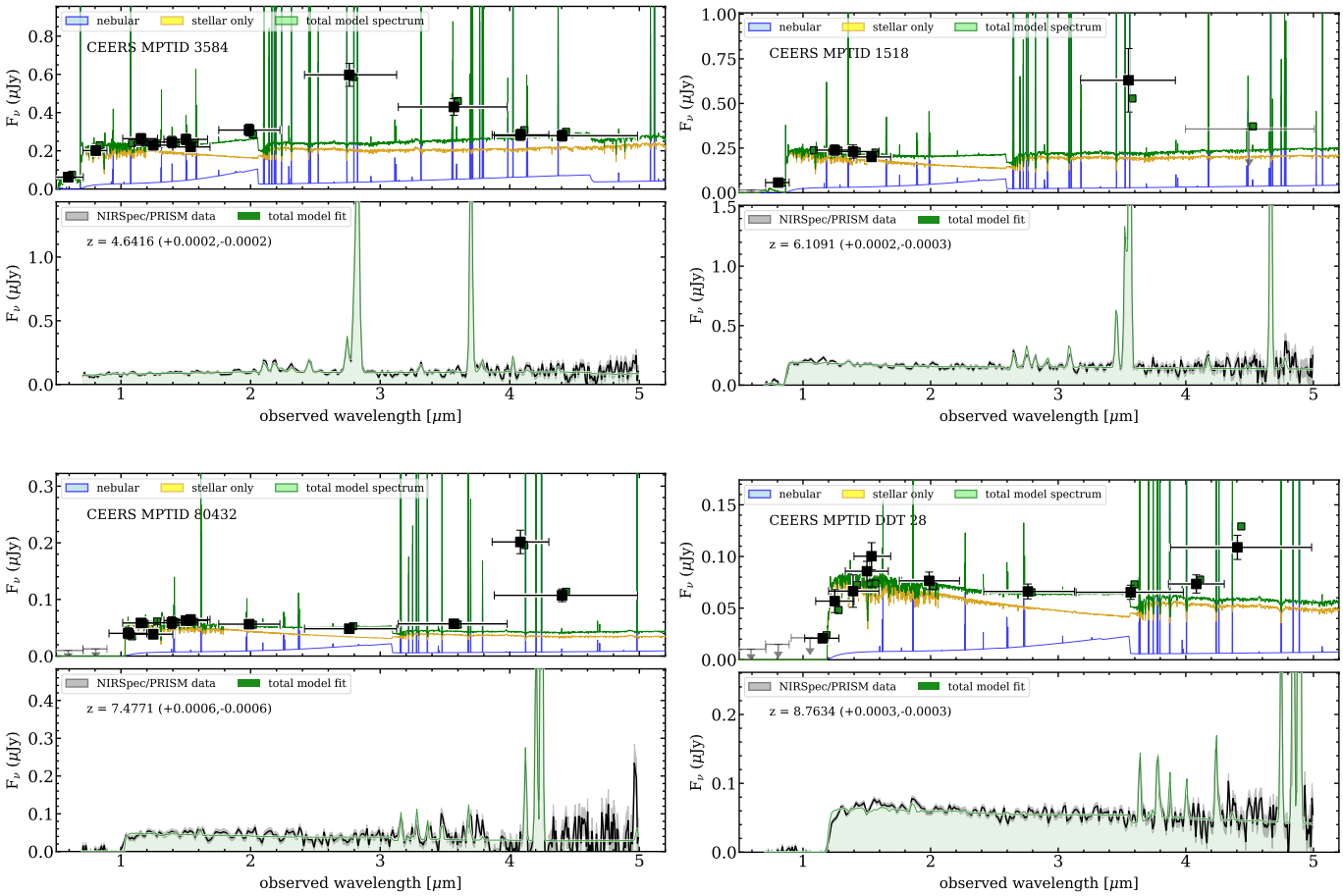


**Figure 2.** Examples SED fits to galaxies in the CEERS sample. Each pair of plots shows the best-fit model for an individual galaxy, labeled by the MPT ID number. In each pair of plots, the top panel shows the model fit to the broadband photometry. The black data points with error bars show the measured flux densities. The curves show a best-fit total model (green) and the contributions to that model from the stellar light (yellow) and nebular emission (blue). The green squares are the model photometry. The bottom panel of each galaxy shows the same model fit (green curve and shading) to the NIRSpec PRISM data (gray).

We then model the strong nebular lines, [O II], [Ne III], [O III], H$\beta$, and H$\alpha$, with Gaussians. Because the [O II] $\lambda\lambda$3727, 2729 doublet is unresolved, we fit it with a single Gaussian component and measure the sum of the two lines. For [O III], in some cases the line is unresolved, especially at the lower end of our redshift distribution, $z \sim 4.5$, which places these lines at $\sim$2.8–3.0 $\mu$m, where the NIRSpec PRISM resolution is $R \sim$ 80–100. We therefore fit both lines simultaneously, forcing them to have the same dispersion and assuming a line ratio of [O III] $\lambda$5008/[O III] $\lambda$4959 = 2.98. We measure H$\alpha$ with a single Gaussian, but note that it is blended with [N II] $\lambda\lambda$6548, 6583 at the resolution of the prism. This is reasonable, as we expect the contribution of [N II] to be [N II]/H$\alpha$ < 10% given the high redshifts and low metallicities of the galaxies in our sample (A. L. Faisst et al. 2018). Furthermore, we adopt $\xi_{\rm ion}$ constraints based on H$\beta$ as this line is accessible with the NIRSpec PRISM data for all galaxies in our sample. Nevertheless, we show below that the $\xi_{\rm ion}$ values measured from H$\beta$ are consistent with those from H$\alpha$ for cases where both lines are available.

In the following analysis, we explore trends with galaxy EWs and emission-line ratios. For the emission-line ratios, we primarily study the ratio of [O III] to [O II], defined here as

$$\mathrm{O_{32}} \equiv \frac{[\mathrm{O\ III}]\,\lambda4959 + [\mathrm{O\ III}]\,\lambda5008}{[\mathrm{O\ II}]\,\lambda3726 + [\mathrm{O\ II}]\,\lambda3729}. \quad (1)$$

We compare our results to other studies that explore trends in the ratio of these sums, available primarily from other space-based spectroscopic studies using the HST and JWST grisms (C. Papovich et al. 2022; L. Shen et al. 2025).

### 3.4. Measuring the Ionizing Production Efficiency

As introduced above (Section 1), the ionizing production efficiency, $\xi_{\rm ion}$, is defined as $\xi_{\rm ion} \equiv Q(H_0)/L_{\rm UV}$, where $Q(H_0)$ is the hydrogen-ionizing production rate in units of s$^{-1}$. $L_{\rm UV} = F_{1500} \times (4\pi D_L^2)(1+z)^{-1}$, is the rest-frame UV continuum luminosity, using the redshift ($z$) and rest-frame UV flux density ($F_{1500}$) derived in Section 3.1. We define the ionizing production rate, $Q$, assuming Case B recombination (C. Leitherer & T. M. Heckman 1995; Y. I. Izotov et al. 2021; M. J. Hayes et al. 2025):

$$Q(\mathrm{H_0}) = 2.12 \times 10^{12}\ \mathrm{s^{-1}}\,(L(H\beta)/\mathrm{erg\ s^{-1}}), \quad (2)$$

where $L$(H$\beta$) is the dust-corrected H$\beta$ luminosity. In cases where we compare to $L$(H$\alpha$), we assume $L$(H$\alpha$) = 2.86$L$(H$\beta$) (D. E. Osterbrock 1989). The definition of $\xi_{\rm ion}$ above implicitly assumes $f_{\rm esc} = 0$; we discuss this further in the sections below.

For galaxies in the redshift range $4.5 < z < 6.8$, we can compare $\xi_{\rm ion}$ derived from H$\beta$ to that derived independently from H$\alpha$. Figure 4 shows that these values are in good agreement on average. Interestingly, the mean (median) ratio is

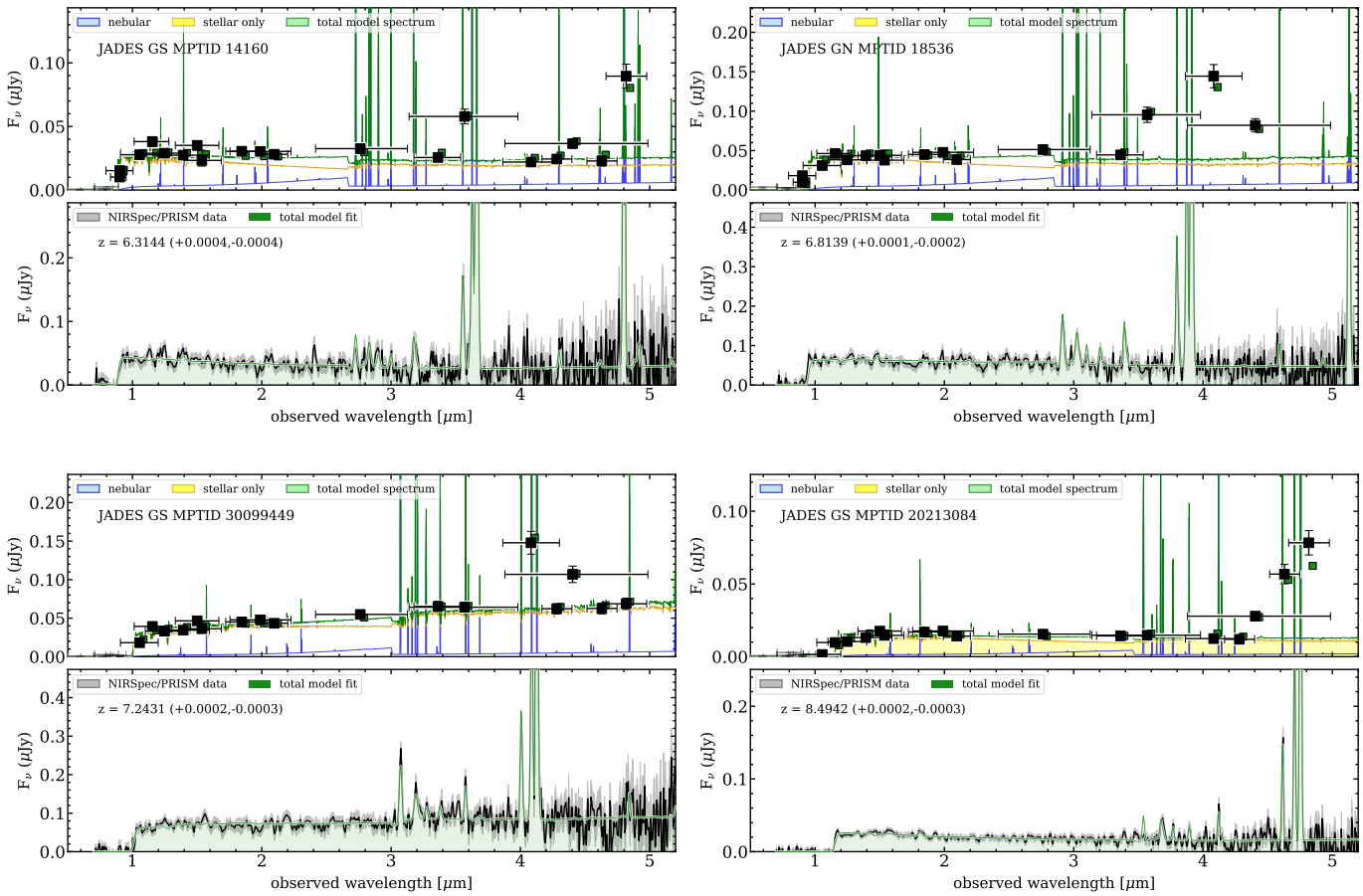


**Figure 3.** Same as Figure 2 but for example galaxies in the JADES sample.

$\xi_{\rm ion}({\rm H}\beta)/\xi_{\rm ion}({\rm H}\alpha) = 1.1$ (1.0), implying that values derived from H$\beta$ are 10% higher in the mean than those from H$\alpha$, although this difference is smaller than the scatter ($\pm$0.4 dex). In some objects, the $\xi_{\rm ion}$ derived from H$\alpha$ is higher than that from H$\beta$, exceeding the scatter. These may be a result of the dust attenuation law, where we have assumed $E(B-V)_{\rm stars} = E(B-V)_{\rm nebular}$ for all galaxies, which is appropriate for young star-forming galaxies (M. Lecroq et al. 2024). However, some studies find higher levels of attenuation in the nebular gas compared to the stellar continuum (e.g., D. Calzetti 2001; K. Kreckel et al. 2013; N. A. Reddy et al. 2015; B. Salmon et al. 2016; C. Robertson et al. 2024), particularly for dustier galaxies (N. A. Reddy et al. 2015). In the latter case, this would *increase* the dust-corrected H$\beta$ luminosity and $\xi_{\rm ion}$. It is also possible that these galaxies have higher ratios of [N II]/H$\alpha$, inflating $\xi_{\rm ion}$(H$\alpha$). It could also be a result of the assumption of Case B recombination (e.g., J. E. Méndez-Delgado et al. 2024; C. Scarlata et al. 2024). Nevertheless, the effect of dust attenuation is low because most of our galaxies have low color excess, $E(B-V) \lesssim 0.3$ (see Appendix A). We therefore adopt the results using $\xi_{\rm ion}$ from H$\beta$, as this line is available for all our galaxies; however, we caution that these results may include a systematic uncertainty of $\sim$10%–20%.

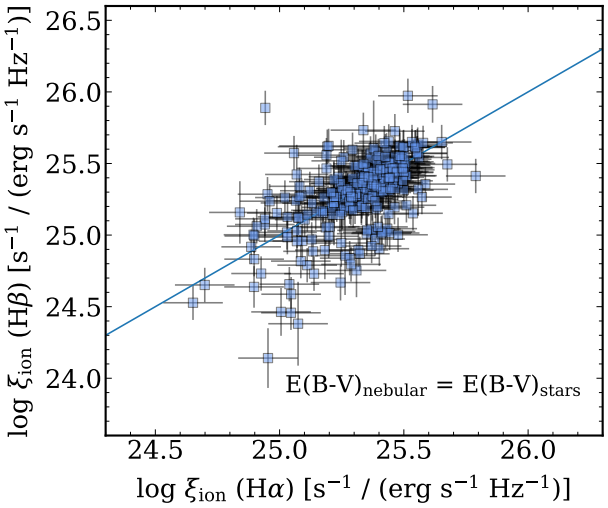


**Figure 4.** Comparison of $\xi_{\rm ion}$ derived from the H$\alpha$ line to that from the H$\beta$ line. The $\xi_{\rm ion}$ values are derived based on each Balmer emission line. In both cases we assume the dust attenuation of the stellar continua is equal to that of the nebular emission, $E(B-V)_{\rm nebular} = E(B-V)_{\rm stars}$. The solid line shows the unity relation. These results show H$\beta$ is a reasonable surrogate for H$\alpha$ when deriving $\xi_{\rm ion}$ for our datasets.

## 4. Results

### 4.1. The Ionizing Production Efficiency of EoR Galaxies

Our first finding is that fainter galaxies are more efficient at producing ionizing radiation, and this efficiency increases with increasing redshift. Moreover, the scatter in this trend is significant. Figure 5 shows the distribution of $\xi_{\rm ion}$ as a function of UV absolute magnitude ($M_{\rm UV}$), color-coded by redshift. We quantify trends by fitting a linear relation between $\xi_{\rm ion}$ and $M_{\rm UV}$ using `LINMIX` (B. C. Kelly 2007) to the data in three redshift bins: $4.5 < z < 5.5$, $5.5 < z < 6.5$, and $6.5 < z < 9.0$. `LINMIX` uses Gaussian mixture models to estimate the linear

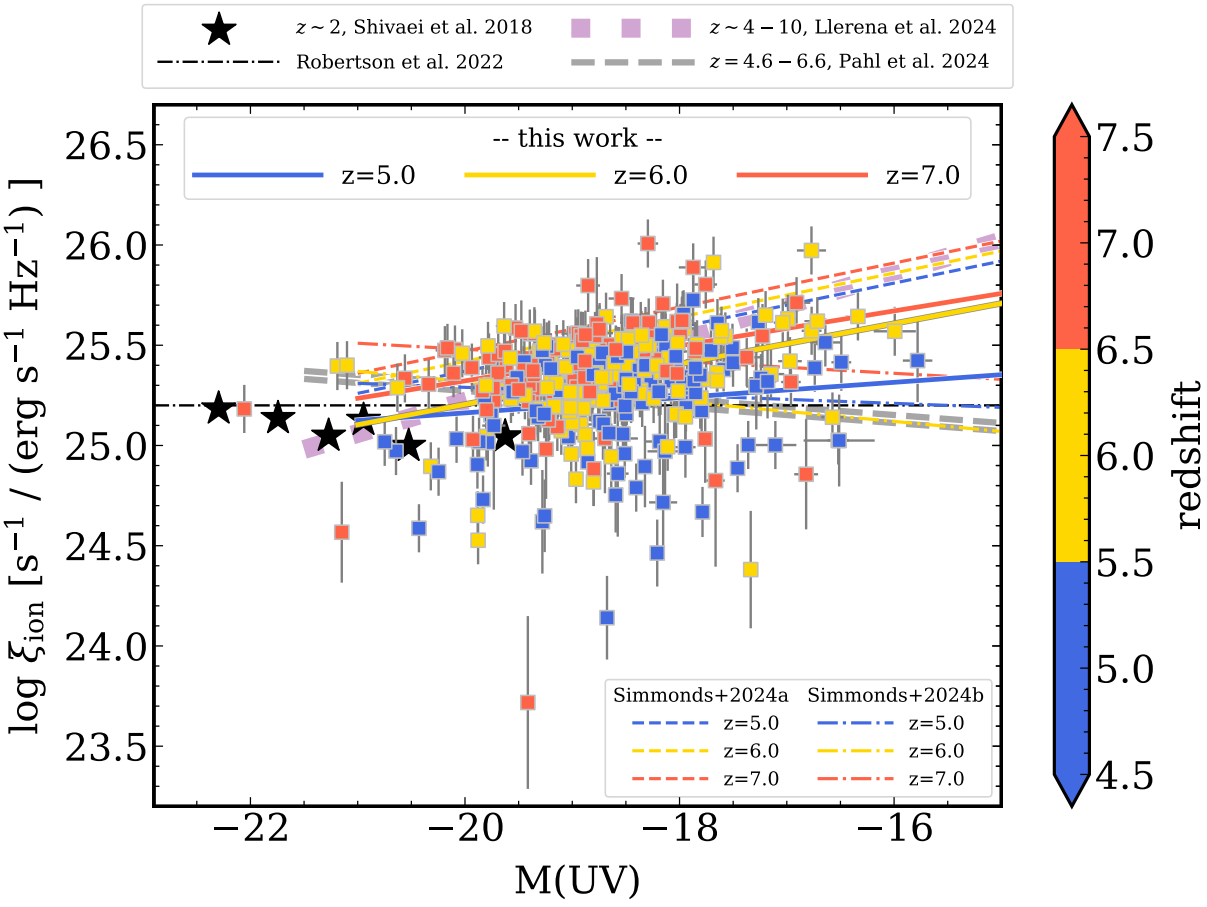


**Figure 5.** UV absolute magnitude, $M_{\rm UV}$, vs. the ionizing photon production efficiency, $\xi_{\rm ion}$. The data points show the results derived from the CEERS and JADES datasets, color-coded by redshift. The solid lines show linear fits to the relation in bins of redshift, as labeled. These are consistent with results derived based on the analysis of photometric broadbands (dashed lines; C. Simmonds et al. 2024a) and other spectroscopic analyses of $4 < z < 10$ (M. Llerena et al. 2025), with some notable differences (e.g., A. Pahl et al. 2025; see text). At the bright end, $M_{\rm UV} \lesssim -20$, our results are similar to the measurements at $z \sim 2$ from I. Shivaei et al. (2018) and the canonical value for stellar populations, $\xi_{\rm ion} = 25.2$, argued by B. E. Robertson et al. (2023).

fit, incorporating uncertainties on the dependent and independent variables and allowing intrinsic scatter in the sample. We fit the data with a linear relation:

$$\log \xi_{\rm ion} = A(z)(M_{\rm UV} + 18) + \log \xi_{\rm ion}^{-18}(z). \quad (3)$$

The results are shown in Figure 5 and tabulated in Table 2. The slopes ($A$) of the relations show slight evidence of evolution with redshift, with $A(z) \simeq 0.04 \pm 0.3$ at $4.5 < z < 5.5$ to $A(z) = (0.09\text{–}0.10) \pm 0.02$ at $6.5 < z < 9.0$. This steepening of the slope may also be indicative of sample incompleteness (discussed further below). The normalization, $\log \xi_{\rm ion}^{-18}$ (defined to be $\log \xi_{\rm ion}$ at $M_{\rm UV} = -18$ mag), increases by a factor of 2 from $\log \xi_{\rm ion}^{-18} = 25.2$ at $4.5 < z < 5.5$ to 25.5 at $6.5 < z < 9.0$, where the statistical uncertainties are 0.02–0.03 dex.

The relations between $\log \xi_{\rm ion}$ and $M_{\rm UV}$ we measure are consistent with previous studies, with some notable differences. At $4.5 < z < 5.5$, this normalization is consistent with the canonical value expected for star-forming stellar populations, $\log \xi_{\rm ion} = 25.2$ (B. E. Robertson et al. 2023), and studies of star-forming galaxies at $z \sim 2$ (I. Shivaei et al. 2018). In the JWST era, studies at higher redshift, $z > 5.5$, find a similar increase in $\xi_{\rm ion}$ compared to what we observe (e.g., H. Atek et al. 2024; C. Simmonds et al. 2024a, 2024b; M. J. Hayes et al. 2025; M. Llerena et al. 2025; A. Pahl et al. 2025). Interestingly, the relation between $\log \xi_{\rm ion}$ and $M_{\rm UV}$ may not be linear. At bright magnitudes, e.g., $M_{\rm UV} \lesssim -19.5$ mag, all galaxies with $4.5 < z < 5.5$ have $\log \xi_{\rm ion}$ below the linear fit, potentially linking them to the galaxy populations seen at $z \sim 2$ (I. Shivaei et al. 2018). This is important and may motivate exploring nonlinear distributions and incorporating the scatter when describing $\xi_{\rm ion}$ at a given $M_{\rm UV}$ and redshift.

**Table 2**
Parameters for Linear Fit between $\xi_{\rm ion}$ and $M_{\rm UV}$ as a Function of Redshift[a]

| $z$ | $A(z)$ | $\log \xi_{\rm ion}^{-18}$ |
|---|---|---|
| $4.5 < z < 5.5$ | $0.04 \pm 0.03$ | $25.24 \pm 0.03$ |
| $5.5 < z < 6.5$ | $0.10 \pm 0.02$ | $25.41 \pm 0.02$ |
| $6.5 < z < 9.0$ | $0.09 \pm 0.02$ | $25.50 \pm 0.03$ |

**Note.**
[a] Parameters are defined in Equation (3).

We quantify the average and scatter of the ionizing production efficiency by fitting a Gaussian to the $\log \xi_{\rm ion}$ distribution in bins of $M_{\rm UV}$ and redshift, with results shown in Figure 6 and Table 3. In all bins the scatter is typically $\sigma(\log \xi_{\rm ion}) \simeq 0.20\text{–}0.30$ dex, consistent with other recent work (e.g., R. Begley et al. 2025; A. Pahl et al. 2025). It is notable that a similar amount of scatter is observed in the $\xi_{\rm ion}$ distributions of $z \sim 2$ galaxies (I. Shivaei et al. 2018). This scatter is important as it tells us that galaxies at these redshifts

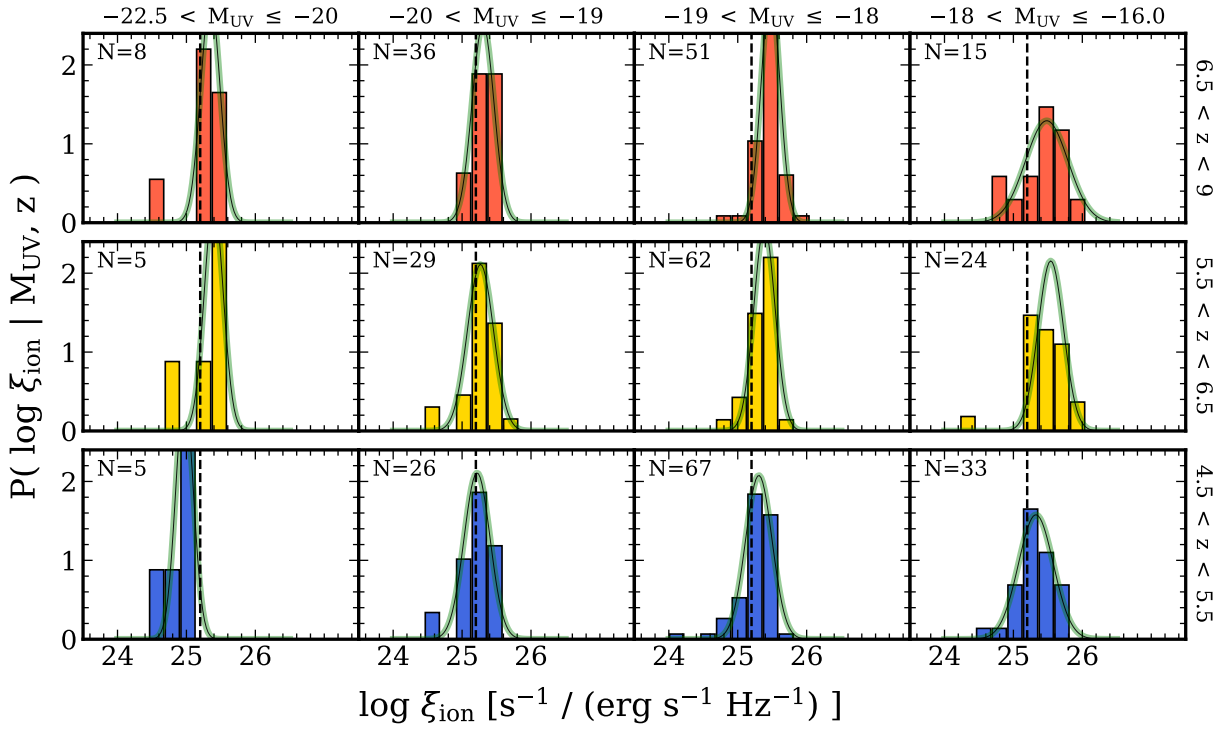


**Figure 6.** Distribution functions for $\log \xi_{\rm ion}$ as a function of redshift, $z$, and UV magnitude, $M_{\rm UV}$, $P(\log \xi_{\rm ion}|M_{\rm UV}, z)$. Each row shows the results binned as a function of redshift (as labeled on the right-hand axis). Each column shows the distribution of $\xi_{\rm ion}$ in bins of $M_{\rm UV}$, as labeled along the top axis. The inset labels provide the number of galaxies in the distribution of each panel. The green curve in each panel shows a Gaussian fit to the distribution, with results given in Table 3. The vertical dashed lines show the canonical $\log \xi_{\rm ion} = 25.2$ value of B. E. Robertson et al. (2023).

**Table 3**
Mean and Scatter in $\log \xi_{\rm ion}$ as a Function of $M_{\rm UV}$ and Redshift[a]

| | $-22 < M_{\rm UV} < -20$ | | | $-20 < M_{\rm UV} < -19$ | | | $-19 < M_{\rm UV} < -18$ | | | $-18 < M_{\rm UV} < -16$ | | |
|---|---|---|---|---|---|---|---|---|---|---|---|---|
| $z$ | $N$ | $\mu$ | $\sigma$ | $N$ | $\mu$ | $\sigma$ | $N$ | $\mu$ | $\sigma$ | $N$ | $\mu$ | $\sigma$ |
| $4.5 < z < 5.5$ | 5 | 24.97 | 0.13 | 26 | 25.22 | 0.19 | 67 | 25.31 | 0.19 | 33 | 25.33 | 0.25 |
| $5.5 < z < 6.5$ | 5 | 25.40 | 0.14 | 29 | 25.27 | 0.19 | 62 | 25.39 | 0.15 | 24 | 25.54 | 0.19 |
| $6.5 < z < 9.0$ | 8 | 25.35 | 0.14 | 36 | 25.30 | 0.16 | 51 | 25.48 | 0.14 | 15 | 25.48 | 0.31 |

**Note.**
[a] The values in the table show the number of galaxies in each bin, $N$, and the Gaussian fits with mean $\mu$ and variance $\sigma^2$ of $\log \xi_{\rm ion}$ in each bin. These fits are illustrated in Figure 6.

produce different rates of ionizing photons at a fixed UV luminosity. This may be a symptom of increased "burstiness" in the star formation histories of galaxies, as has been suggested from photometric studies (C. Simmonds et al. 2024b; J. W. Cole et al. 2025; R. Endsley et al. 2025). For the mode (peak) of the $\log \xi_{\rm ion}$ distributions, these increase with decreasing $M_{\rm UV}$ and increasing redshift. This says that, on average, fainter galaxies are more efficient at producing ionizing photons, with this efficiency increasing at higher redshifts.

Our sample may be biased by the fact that it requires spectroscopic confirmation. Recent studies using photometric samples demonstrate this bias (C. Simmonds et al. 2024b; R. Begley et al. 2025). Figure 5 shows the $\xi$–$M_{\rm UV}$ relation from C. Simmonds et al. (2024b), which found a flat or decreasing relation between $\xi$ and $M_{\rm UV}$. R. Endsley et al. (2025) used photometric samples and found that $\xi_{\rm ion}$ declines with UV luminosity, opposite to the trend in our data, which they interpret as evidence that "post burst" galaxies have lower $\xi_{\rm ion}$ values, weaker emission lines, and fainter UV magnitudes. However, as stated above, these photometric samples could be biased in that galaxies with weaker emissions lines are more difficult to interpret. While these are consistent with our distributions $4.5 < z < 5.5$, they deviate at higher redshifts. To test this potential bias will require deeper spectroscopy of fainter $M_{\rm UV}$ galaxies at these redshifts.

### 4.2. The Inferred LyC Escape Fractions of EoR Galaxies

Another of our main findings is that the inferred $f_{\rm esc}$ values for $4.5 < z < 9.0$ galaxies are on average low, with no evidence of evolution with redshift or $M_{\rm UV}$. Figure 7 shows the distribution of $f_{\rm esc}$ as a function of $M_{\rm UV}$ for the galaxies in our CEERS and JADES samples. The lines in Figure 7 show the median values of $f_{\rm esc}$ in the three redshift bins. We list the median values and the scatter, derived from the normalized median absolute deviation, $\sigma_{\rm NMAD}$, in Table 4.

The median $\log f_{\rm esc}$ values are similar across all redshift bins, with median $\log f_{\rm esc}$ ranging from $-2.5$ to $-2.4$, with a scatter of $\sigma_{\rm NMAD} = 0.2$–$0.3$. This implies a median $f_{\rm esc}$ of less than 1% (however, this is misleading when considering only

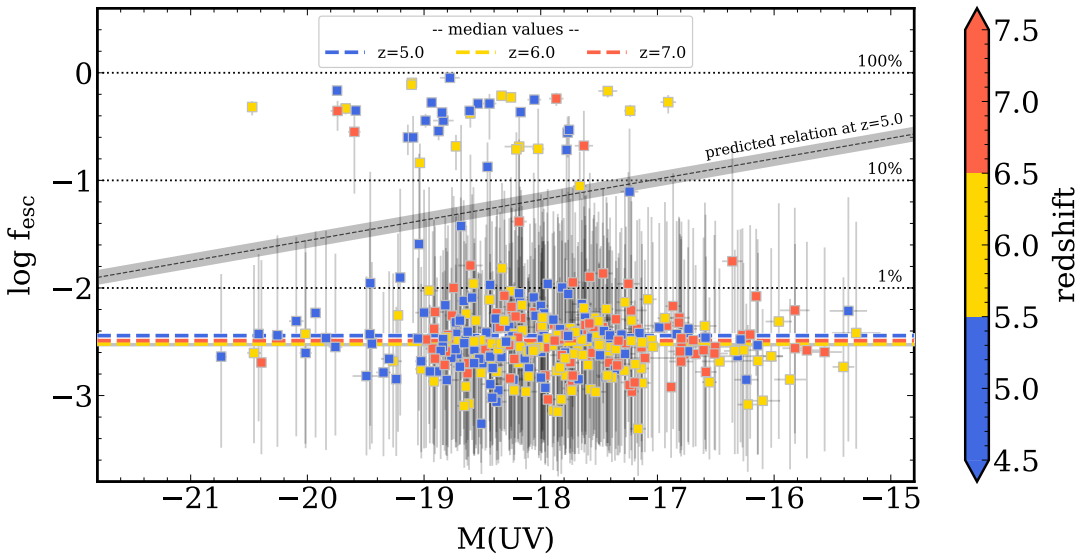


**Figure 7.** UV magnitude, $M_{\rm UV}$, vs. inferred LyC escape fraction, $f_{\rm esc}$. The data points show the median values for the galaxies in the JADES and CEERS samples, color-coded by redshift. The error bars show the 16th–84th percentile range for each galaxy. The horizontal dotted lines denote escape fractions of 1%, 10%, and 100%. The thicker horizontal lines show medians derived from the samples in bins of redshift. These do not include uncertainties on the medians, which are 0.2–0.3 dex (see text). Fewer than 20% of galaxies at $z > 4$ have inferred $f_{\rm esc}$ values greater than a few percent. This contrasts with predictions inferred from the UV spectral slopes and UV magnitudes for low-redshift galaxies, where the diagonal line shows the empirical predictions for $z = 5$ derived from LzLCS at $z \sim 0.3$ (J. Chisholm et al. 2019). These predictions shift to higher $f_{\rm esc}$ for higher-redshift galaxies.

the medians; see Section 5.2). Comparing the numbers, 89% of galaxies in our sample have $\log f_{\rm esc} < -1$ and 82% have $\log f_{\rm esc} < -2$. This implies that the majority of the galaxies in our sample favor low $f_{\rm esc}$. This is consistent with a recent finding by E. Giovinazzo et al. (2025) based on an independent analysis using only JWST spectroscopy, that the majority of galaxies, $\gtrsim$95%, have no statistical evidence for high $f_{\rm esc}$, though those authors found a much higher fraction of galaxies with median $f_{\rm esc} > 10\%$, which we disfavor from our analysis.

We reiterate the important caveat that we are constraining the *inferred* LyC escape fractions from the SED modeling. This is the best we can do, given that direct measurements of $f_{\rm esc}$ are not possible because the density of H I absorbers makes the IGM optically thick to LyC emission at $z \gtrsim 4$ (A. K. Inoue et al. 2014). Our results indicate that there is no evidence for most galaxies having high $f_{\rm esc}$, as nearly all LyC photons produced need to be reprocessed to account for strength of the nebular emission lines (see also Appendix B). It is therefore prudent to consider what features in the modeling are sensitive to the escape fraction, and what aspects of the data are driving the fits to favor low $f_{\rm esc}$.

Figure 8 shows SED fits to the spectra for two of the galaxies from Figure 2. Both of these have solutions that favor $f_{\rm esc} \lesssim 1\%$. CEERS 1518 has $\log f_{\rm esc} = -2.79^{+0.88}_{-0.87}$, with only 3.5% of the likelihood having $f_{\rm esc} > 3\%$ (and no likelihood of $f_{\rm esc} > 10\%$). CEERS DDT 28 has $\log f_{\rm esc} = -2.22^{+0.76}_{-1.17}$, with 17% of the likelihood with $f_{\rm esc} > 1\%$ (but only 2% of the likelihood above $f_{\rm esc} > 10\%$). These values are representative for the majority of galaxies in the samples, as indicated by the error bars on $f_{\rm esc}$ in Figure 7.

The models in Figure 8 include both a "best-fit" model (a model selected to have near-maximum likelihood; blue solid lines) and a model where we forced a higher $f_{\rm esc} = 30\%$ (red dashed lines). In the latter case, it is evident that the model underpredicts the strength of the emission lines, particularly H$\beta$+[O III] (and H$\alpha$ in the case of CEERS 1518). This model also underpredicts the rest-UV ($\sim$1500–3000 Å) continuum, because it has a lower contribution from the nebular continuum (H. Katz et al. 2025). These factors lead the SED fitting to disfavor models with higher $f_{\rm esc}$ values.

**Table 4**
Medians and $\sigma_{\rm NMAD}$ of the $\log f_{\rm esc}$ Values in Bins of Redshift

| $z$ | Median $\log f_{\rm esc}$ | $\sigma_{\rm NMAD}$ |
|---|---|---|
| $4.5 < z < 5.5$ | −2.44 | 0.31 |
| $5.5 < z < 6.5$ | −2.52 | 0.32 |
| $6.5 < z < 9.0$ | −2.49 | 0.24 |

Motivated by these examples, in Appendix B we consider how well the SED modeling can recover $f_{\rm esc}$ for simulated galaxies. As expected, as $f_{\rm esc}$ increases, the strength of the emission lines decreases compared to the continuum. As the continuum drives the number of produced ionizing photons, fitting the weaker emission lines requires higher $f_{\rm esc}$. We show that for model galaxies with properties similar to those in our sample, simulating an increase in $f_{\rm esc}$ allows the SED fitting to recover these values (see Appendix B).

### 4.3. Constraints on the Cosmic Ionizing Rate Density

Our measurements of the ionizing production efficiency, $\xi_{\rm ion}$, and the constraints on the LyC escape fraction, $f_{\rm esc}$, allow us to compute the cosmic ionization production rate density (also called the emissivity), $\dot{n}_{\rm ion}$, which is the rate of ionizing photons produced per cubic (comoving) Mpc. This quantity is derived by integrating the UVLF, $\phi(M_{\rm UV})$, multiplied by the product of ($f_{\rm esc} \times \xi_{\rm ion} \times L_{\rm UV}$); that is,

$$\dot{n}_{\rm ion} = \int \phi(M_{\rm UV}) L_{\rm UV} \xi_{\rm ion} f_{\rm esc} \; dM_{\rm UV}. \quad (4)$$

We use a Monte Carlo simulation to compute $\dot{n}_{\rm ion}$, which enables sampling both the uncertainties in the UVLF parameters and the full measured distributions of $\xi_{\rm ion}$ and $f_{\rm esc}$ as a function of $M_{\rm UV}$ and redshift. In each iteration of the

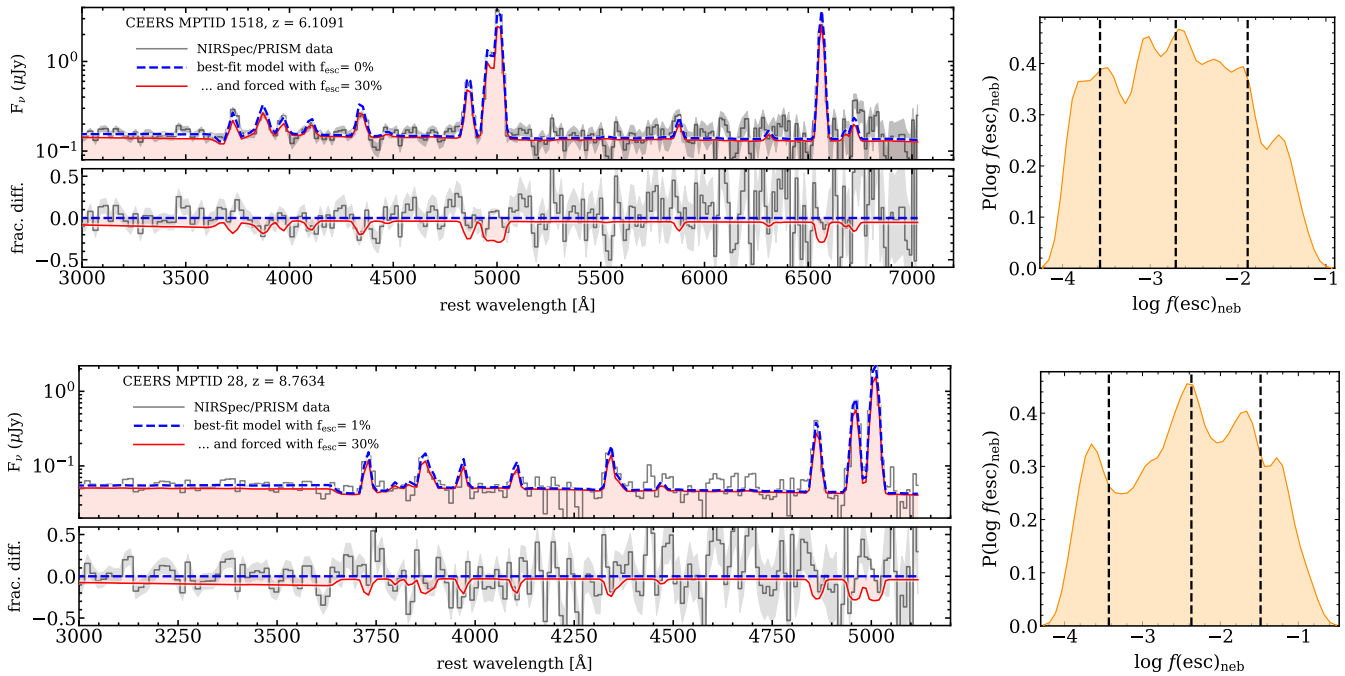


**Figure 8.** Example of how the $f_{\rm esc}$ impacts the SEDs for two galaxies (top and bottom rows) from Figure 2 with low inferred $f_{\rm esc}$ from the SED fitting. In each galaxy, the left panels show the NIRSpec PRISM data along with the best-fit from the SED fitting (solid blue line), which has $f_{\rm esc} \ll 1\%$. The model illustrated by the red dashed line shows the case if we force a high escape fraction, $f_{\rm esc} = 30\%$. The bottom panels show the relative flux difference compared to the best-fit model, $\Delta F_\nu / F_\nu$. In the case of the $f_{\rm esc} = 30\%$ models, clear differences are evident, particularly in the emission lines, but also in the nebular continuum. These features are not as strong as expected given the ionizing continuum from the stellar population. The right-hand panels show the one-dimensional distributions for $\log f_{\rm esc}$ for each galaxy. The vertical dashed lines show the 16th, 50th, and 84th percentiles.

Monte Carlo, we first draw a sample of galaxies with $M_{\rm UV}$ chosen to reproduce the UVLF of S. L. Finkelstein et al. (2022) at different redshifts, $z \in (5, 6, 7, 8)$, employing redshift bins that match those of the UVLF. We also extend these simulations to higher redshift using the UVLF of C. T. Donnan et al. (2024) to consider the redshift evolution of the cosmic ionized-hydrogen fraction, $x_e$ (see Section 5.5). In each instance of the simulation, we vary the parameters of the UVLF within the values and covariances. In this way, the total number of galaxies, as well as the number of galaxies per unit magnitude, incorporates the full range of uncertainties in the UVLF.

Second, for each galaxy in the simulated sample, we draw a random value for $\xi_{\rm ion}$ from our measured distribution, $P(\xi_{\rm ion}|M_{\rm UV}, z)$, based on the galaxy's $M_{\rm UV}$ and $z$, using the empirically measured distributions (Table 3). For $f_{\rm esc}$, we select a value of $f_{\rm esc}$ by taking at random a (real) galaxy from our sample at similar $M_{\rm UV}$ and $z$ as the simulated galaxy, and drawing a value from its $P(\log f_{\rm esc}|M_{\rm UV}, z)$ distribution. In this way, each simulated galaxy is assigned $\xi_{\rm ion}$ and $f_{\rm esc}$ values sampled from the measured galaxy distribution functions.

We repeated the Monte Carlo simulation 4000 times for each of two cases: one assuming a faint-end cutoff of the UVLF at $M_{\rm UVcut} = -16$, which is the observational limit of our dataset, and one assuming $M_{\rm UVcut} = -14$, near the lowest value to which the UVLF has been measured (H. Atek et al. 2024). In the latter case, we must extrapolate our relations, using the $\xi_{\rm ion}$ and $f_{\rm esc}$ distributions for galaxies with $M_{\rm UV} = -16$ for all galaxies fainter than this value. We then calculate $\dot{n}_{\rm ion}$ as a function of redshift using Equation (4) for each simulation. We take the median $\dot{n}_{\rm ion}$ of the distribution as the quoted value, with the 16th–84th percentile range as the error.

The results of the Monte Carlo simulation are shown in Figure 9 and Table 5. The figure compares the $\dot{n}_{\rm ion}$ values to the rate needed to sustain an ionized universe at a given redshift from P. Madau et al. (1999). One of the remaining uncertainties is the "clumping factor" of the gas in the IGM, $C$, for which we must rely on predictions from simulations (e.g., P. Madau et al. 1999; K. Finlator et al. 2011; A. H. Pawlik et al. 2015; F. B. Davies et al. 2024). Figure 9 shows that the production rate of ionizing photons needed for reionization increases with this clumpiness factor, and that if we include galaxies with $M_{\rm UV} < -16$ ($-14$) we do not reach this level until $z \sim 5$ ($z \sim 6$) for $C \sim 3$.

## 5. Discussion

### 5.1. Why Are the Ionizing Production Efficiencies of EoR Galaxies High?

In Section 4.1, we showed that the ionizing production efficiency in our samples increases for fainter galaxies and toward higher redshift. This echoes trends observed from other JWST studies that find high values, $\log \xi_{\rm ion} = 25 - 26$, for galaxies at $z \simeq 7$–$8$. This includes both studies that used SED fitting of JWST imaging data to infer $\xi_{\rm ion}$ (e.g., G. Prieto-Lyon et al. 2023; C. Simmonds et al. 2024a, 2024b; R. Begley et al. 2025; R. Endsley et al. 2025) and spectroscopic studies that find similar trends of an increase in $\xi_{\rm ion}$ for EoR galaxies (e.g., H. Atek et al. 2024; A. Calabrò et al. 2024; S. Mascia et al. 2024; A. Saxena et al. 2024; M. J. Hayes et al. 2025; M. Llerena et al. 2025; A. Pahl et al. 2025). Ours is the first to estimate $\xi_{\rm ion}$ by combining photometric and spectroscopic data in a consistent treatment.

The finding that $\xi_{\rm ion}$ is higher at high redshifts seems robust, given that most studies use different methods, assumptions,

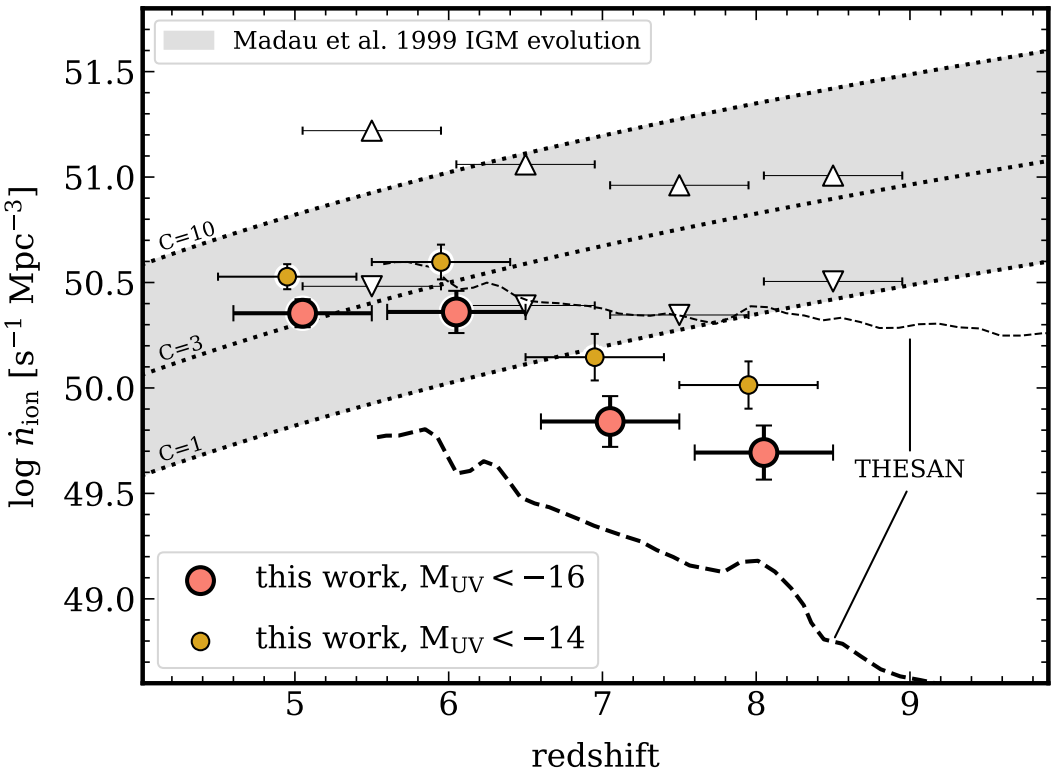


**Figure 9.** Evolution of $\dot{n}_{ion}$ as a function of redshift. The large circles show the results from our analysis of the JADES and CEERS samples, where we integrate the UVLF to $M_{UV} < -16$ (large circles) and $M_{UV} < -14$ (small circles). The vertical error bars show the 16th–84th percentile range, and the horizontal error bars show the bounds of the redshift bin. The triangles show results from the analysis of JWST photometric data with different assumptions for the LyC escape fractions from C. Simmonds et al. (2024a; upward triangles) and C. Simmonds et al. (2024b; downward triangles). The shaded region shows the $\dot{n}_{ion}$ required to reionize the IGM at a given redshift for different assumptions of the H I clumping factor $C$ (P. Madau et al. 1999). The dashed lines show predictions from the THESAN simulation for the global galaxy population (light line) and galaxies with $\log M_*/M_\odot = 8 - 9$ (thick line; J. Y. C. Yeh et al. 2023).

**Table 5**
Measured Ionizing Photon Production Rate Density

| | $\log(\dot{n}/\mathrm{s}^{-1}\ \mathrm{Mpc}^{-3})$ | |
|---|---|---|
| $z$ | $(M_{UV} < -16)$ | $(M_{UV} < -14)$ |
| 5.0 | $50.52 \pm 0.08$ | $50.72 \pm 0.07$ |
| 6.0 | $50.59 \pm 0.09$ | $50.85 \pm 0.08$ |
| 7.0 | $50.29 \pm 0.11$ | $50.59 \pm 0.10$ |
| 8.0 | $50.10 \pm 0.13$ | $50.49 \pm 0.11$ |

and samples. For example, M. J. Hayes et al. (2025) considered the properties of stacked (average) NIRSpec PRISM spectra for galaxies at $4 < z < 10$, finding $\log \xi_{ion} \simeq 25.2 - 25.7$, with a strong correlation between $\xi_{ion}$ and many signatures of LyC escape. Using individual galaxy spectra, M. Llerena et al. (2025) measured $\xi_{ion}$ from Balmer emission-line measurements from NIRSpec PRISM and $R \sim 1000$ data, combined with photometric modeling to obtain $L_{UV}$ for galaxies at $4 < z < 10$. Their results yield results similar to those here, at least in the mean (see Figure 5).

Not all analyses find that $\xi_{ion}$ increases with decreasing UV luminosity, which may reflect systematic uncertainties or selection effects. A. Pahl et al. (2025) measured the evolution of $\xi_{ion}$ using JWST spectroscopy for galaxies at $1.06 < z < 6.71$, finding that $\xi_{ion}$ is higher for UV-luminous galaxies and declines with decreasing UV luminosity. This may be related to sample selection, as A. Pahl et al. (2025) required $>3\sigma$ detections in both the H$\beta$ and H$\alpha$ lines, or to differences in the SED modeling and spectroscopic slit-loss corrections. Studies using multiband imaging data including medium-band photometry also find that UV-fainter galaxies show lower $\xi_{ion}$ (C. Simmonds et al. 2024b; R. Endsley et al. 2025). One explanation for this is that some fainter galaxies are postburst, which would have lower $\xi_{ion}$ and fainter UV magnitudes (R. Endsley et al. 2025). Such galaxies could be missed by spectroscopic surveys, and also suffer from larger photometric redshift uncertainties. This highlights the potential for selection effects in spectroscopic samples. Testing these selection effects will require deeper JWST/NIRSpec observations (e.g., M. Dickinson et al. 2024).

An increase in $\xi_{ion}$ requires a greater ionizing production rate, $Q(H_0)$, per unit far-UV continuum luminosity, $L_{UV}$. This occurs when galaxies either have a higher fraction of O-type stars or when these stars have hotter effective temperatures, or both. I. Shivaei et al. (2018) measured empirical trends for galaxies at $z \sim 0$–2, showing that $\xi_{ion}$ increases with lower dust content, stellar population age, and metallicity. Higher effective temperatures are predicted as a consequence of lower-metallicity stars, which lowers the opacity in stellar photospheres, leading to higher LyC production (see, e.g., L. Y. A. Yung et al. 2020b; S. Mascia et al. 2024). Studies using JWST observations of nebular emission find that the gas-phase metallicity declines with increasing redshift (e.g., M. Curti et al. 2023; J. R. Trump et al. 2023). Assuming this trend extends to lower stellar metallicities, it could provide a physical explanation for the increase in galaxies' $\xi_{ion}$ as metallicity declines with redshift (M. Llerena et al. 2025).

A related consideration is that galaxies in our samples may be dominated by young, $\lesssim$5 Myr stellar populations, which

would increase the relative number of O-type stars. This could be a consequence of "burstier" star formation histories in these galaxies, which have been reported in some studies using JWST (e.g., C. Simmonds et al. 2024b; J. W. Cole et al. 2025; R. Endsley et al. 2025; T. J. Looser et al. 2025). Indeed, L. Y. A. Yung et al. (2020b) show that young stellar populations, with ages $\lesssim$10 Myr, are required to maintain $\log \xi_{\rm ion} > 25.5$, without the need to invoke changes to the IMF. In nearby galaxies, the age of H II regions correlates inversely with H$\alpha$/UV and EW(H$\alpha$) (F. Scheuermann et al. 2023). If most of our galaxies are experiencing bursts, and if the frequency of bursts increases with redshift (as argued by, e.g., J. W. Cole et al. 2025), then this provides a physical explanation for the trends in our sample. It may be that galaxies experiencing lulls in their star formation have lower $\xi_{\rm ion}$, which would potentially be underrepresented in spectroscopic samples such as ours (see, e.g., T. J. Looser et al. 2024). C. Simmonds et al. (2024b) considered this by using a mass-complete photometric sample that potentially includes objects with weaker emission lines. They found an increase in the scatter of $\xi_{\rm ion}$, including a tail of objects with lower $\xi_{\rm ion}$, primarily at $z \lesssim 7$, but that $\xi_{\rm ion}$ remains high, $\log \xi_{\rm ion} \simeq 25.4$, at $M_{\rm UV} = -18$. R. Begley et al. (2025) obtain similar results.

It is therefore interesting to consider which properties of galaxies correlate with $\xi_{\rm ion}$ at higher redshifts. Figure 10 shows the relation between the [O III]/[O II] ratio, EWs of H$\beta$ and [O III], and $\xi_{\rm ion}$ for the galaxies in our samples. The $\xi_{\rm ion}$ of our galaxies increases with (1) increasing [O III]/[O II] ratio, (2) increasing EW(H$\beta$), and (3) increasing EW([O III]). Comparing our sample to galaxies at redshifts $1 < z < 3$ (I. Shivaei et al. 2018; L. Shen et al. 2025), the relation between $\xi_{\rm ion}$ and [O III]/[O II] appears nearly unchanged with redshift, consistent with other JWST studies (e.g., M. Llerena et al. 2025). The relation between EW([O III]) and $\xi_{\rm ion}$ for our samples is also shallower than those of "extreme" line emitters at lower redshift (M. Tang et al. 2019), indicating EoR galaxies may not fall in this category. [O III]/[O II] correlates with the ionization parameter, with a secondary dependence on metallicity such that, at a fixed ionization parameter, lower-metallicity galaxies will have a higher [O III]/[O II] ratio (A. L. Strom et al. 2018; C. Papovich et al. 2022). This can explain why, at a fixed [O III]/[O II] ratio, galaxies at higher redshift have higher $\xi_{\rm ion}$, as they are expected to have lower metallicities. Interestingly, the higher [O III]/[O II] ratios observed in some galaxies at fixed EW(H$\beta$), relative to lower-redshift samples (L. Shen et al. 2025), may indicate the presence of radiation-bounded H II regions (A. Plat et al. 2019).

### 5.2. Why Are the Inferred Escape Fractions of EoR Galaxies Low?

In Section 4.2, we showed that the inferred escape fractions of $4.5 < z < 9.0$ galaxies are low—a few percent or less on average for most galaxies. Based on SED fitting, the $f_{\rm esc}$ values imply that the strength of the emission lines requires nearly all of the ionizing photons produced by the stellar population to be absorbed within H II regions and reprocessed into nebular emission. Therefore, the observable factors driving this relation are the relative shapes of the rest-frame far-UV and optical continua, and the strength of the emission lines themselves. As shown above (Section 4.2), variations in $f_{\rm esc}$ influence the relative strengths of these components (see also Appendix B). Nevertheless, an underlying uncertainty in this analysis is that $f_{\rm esc}$ assumes the stellar populations and nebular emission reflect reality. We discuss this further below (Section 5.4), but ultimately to test the details of these models will require analyses of a multitude of emission lines for individual galaxies at these redshifts. This is beyond the scope of the present work, but may be possible with forthcoming datasets from JWST (T. A. Hutchison et al. 2024; C. Papovich et al. 2024).

Section 4.2 also shows that there is no strong evidence for evolution in $f_{\rm esc}$ with either redshift or $M_{\rm UV}$ (see Section 4.2, Figure 7). This is striking given the expectations based on low-redshift studies. Figure 7 shows the predicted relation for $z = 5$ galaxies from J. Chisholm et al. (2022), based on correlations among $f_{\rm esc}$, $M_{\rm UV}$, and the UV spectral slope ($\beta_{\rm UV}$) from LzLCS. When applied to galaxies at $z > 5$ these relations predict a high $f_{\rm esc}$, which increases with redshift, exceeding 5% (10%) for galaxies at $z > 5$ with $M_{\rm UV}$ values fainter than $-19$ ($-17.5$) mag, consistent with findings from studies that apply these relations to EoR galaxies from JWST data (M. W. Topping et al. 2022; F. Cullen et al. 2023; S. Mascia et al. 2024; M. J. Hayes et al. 2025). These predictions favor even higher $f_{\rm esc}$ values for galaxies into the EoR, $z > 6$–7 (see also N. Choustikov et al. 2024, and discussion below).

At low redshift, $z \sim 0.3$, correlations have been measured between various galaxy properties and $f_{\rm esc}$ (e.g., J. Chisholm et al. 2022; S. R. Flury et al. 2022b). Figure 11 shows the relation between $\beta_{\rm UV}$ and EW(H$\beta$), $f_{\rm esc}$ and $\beta_{\rm UV}$, $f_{\rm esc}$ and EW(H$\beta$), and $f_{\rm esc}$ and log[O III]/[O II] for our sample and for LzLCS galaxies at $z \sim 0.3$. In general, no trend is seen between bluer $\beta_{\rm UV}$ and higher $f_{\rm esc}$ in the galaxies in our samples. Notably, a small fraction of our sample appears to follow the trend seen in LzLCS, of $f_{\rm esc}$ increasing with decreasing (bluer) $\beta_{\rm UV}$, implying that some galaxies may follow the relation seen in low-redshift galaxies. Also of interest is that in our samples the EoR galaxies with the highest EW(H$\beta$) also have the lowest $f_{\rm esc}$ values. This contrasts somewhat with the $z \sim 0.3$ samples, which show a trend between increasing EW(H$\beta$) and $f_{\rm esc}$ (S. R. Flury et al. 2022b; also illustrated in Figure 11). The main reason for this is that in the SED modeling strong EW(H$\beta$) requires most of the LyC photons to be absorbed (and therefore not to escape). We also observe no correlation between ionizing parameter, tracked by [O III]/[O II], H$\beta$, and $f_{\rm esc}$, in contrast to the measurements at $z \sim 0.3$ (S. R. Flury et al. 2022b). This may indicate there is a difference in the physical conditions between galaxies in the EoR and ionizing galaxies at $z \sim 0.3$. Other predictive relations between $f_{\rm esc}$ and multivariate galaxy properties such as $\beta_{\rm UV}$, $L(H\beta)$, O32, or ([O III]+[O II])/H$\beta$ (N. Choustikov et al. 2024; A. E. Jaskot et al. 2024) show no correlation with the $f_{\rm esc}$ values we measure. Interestingly, however, applying these to our sample, both multivariate relations derived empirically (A. E. Jaskot et al. 2024) and from simulations (N. Choustikov et al. 2024) favor low *average* values of $\langle f_{\rm esc} \rangle \simeq 4\%$, equal to the mean value from our analysis. However, these studies do *not agree* on which galaxies exhibit high or low $f_{\rm esc}$ as the distributions show no correlation (using the medians, we obtain 0.0032 for our analysis, compared with 0.0031 and 0.0082 for A. E. Jaskot et al. 2024 and N. Choustikov et al. 2024, respectively). Why this is the case is not clear. Therefore, the multivariate measures predict a low

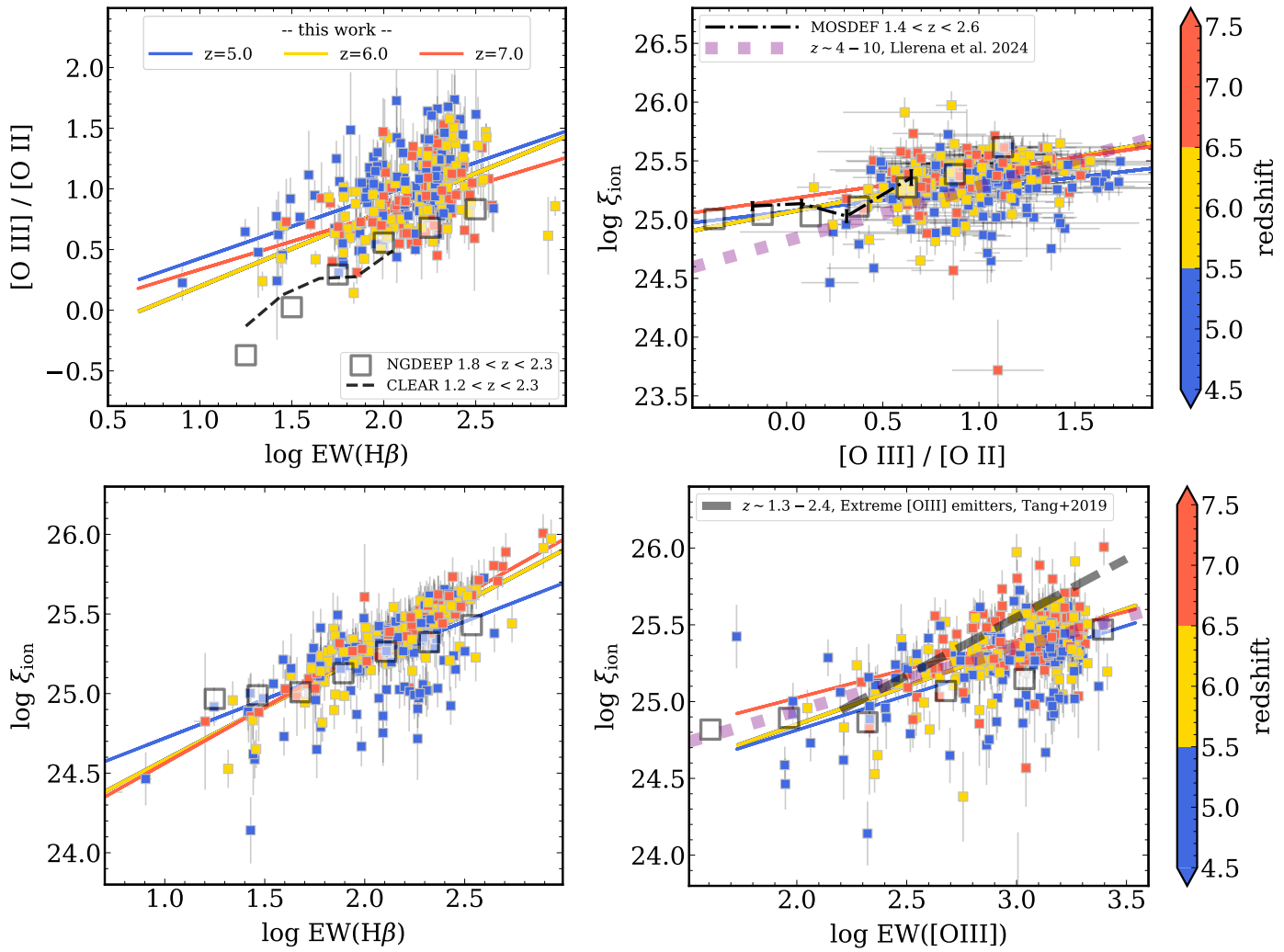


**Figure 10.** Top left: EW of H$\beta$ vs. [O III]/[O II] ratio. The data points show the JADES and CEERS galaxies, color-coded by redshift. Top right: [O III]/[O II] emission-line ratio vs. ionizing photon production efficiency, $\xi_{\rm ion}$. Bottom left: EW(H$\beta$) vs. ionizing photon production efficiency. Bottom right: EW([O III]) vs. ionizing photon production efficiency. In all plots, the data points show the JADES and CEERS galaxies, color-coded by redshift. The solid lines show fits to the different redshift samples (as labeled). The thick purple dashed line shows the relations measured at $4 < z < 10$ by M. Llerena et al. (2025), which are consistent with the measurements here. The black dotted–dashed line shows the relation from MOSDEF at $1.4 < z < 2.6$ (I. Shivaei et al. 2018), and the heavy gray dashed line shows the relation for extreme [O III] emitters at $1.3 < z < 2.4$ (M. Tang et al. 2019). The large open squares show measurements from NGDEEP JWST slitless spectroscopy at $1.2 < z < 2.3$ (L. Shen et al. 2025) and the black dashed line shows the relation from CLEAR HST slitless spectroscopy at $1.2 < z < 2.3$ (C. Papovich et al. 2022).

average $f_{\rm esc}$ for the population, but they disagree on the details. We plan to study these differences in future work.

### 5.3. On the Evolution of the Volume-averaged Escape Fraction

In Section 4.3, we calculated $\dot{n}_{\rm ion}$ using a Monte Carlo simulation. This modeling accounted for the fact that, for most galaxies, the $f_{\rm esc}$ distribution functions, $P(\log f_{\rm esc})$, are broad. This is apparent by looking at the 16th–84th percentile range for individual galaxies in Figure 7. While the distances between the 16th to 50th percentiles and between the 50th to 84th percentiles are similar in logarithmic spacing, the distance from the median to the 84th percentile is substantially larger in *linear* spacing than that from the median to the 16th percentile. This means that a distribution drawn from $P(\log f_{\rm esc})$ randomly for each galaxy will, *on average*, have an expectation value higher than the median from the $P(\log f_{\rm esc})$ likelihood.

Figure 12 illustrates this effect. The figure shows the distribution of the median $\log f_{\rm esc}$ values for galaxies in our sample at $6.5 < z < 9.0$ (yellow shaded histogram). The mean of these medians is $\langle f_{\rm esc} \rangle = 0.015$. However, this should *not* be confused with the expectation value of $f_{\rm esc}$ for the galaxies. For the latter, we can then recompute the distribution if we randomly draw a $\log f_{\rm esc}$ value from the $P(\log f_{\rm esc})$ of each galaxy, which we show as the red shaded histogram in the figure. Because the tail of possible values skews toward higher $f_{\rm esc}$, the result is similarly skewed. The mean of this resampled distribution is $\langle f_{\rm esc} \rangle = 0.03$, a factor of 2 higher. This highlights the importance of considering the full range of $f_{\rm esc}$ probability distribution functions, $P(\log f_{\rm esc})$, from the posteriors of the SED fitting when considering the global escape fraction.

Following J. B. Muñoz et al. (2024), we calculate the *volume-averaged* escape fraction as the ratio of $\dot{n}_{\rm ion}$ using the measured distribution of $f_{\rm esc}$ to the value assuming all of the ionizing radiation escapes, $f_{\rm esc} = 1$; that is,

$$\langle f_{\rm esc} \rangle = \frac{\dot{n}_{\rm ion}(f_{\rm esc})}{\dot{n}_{\rm ion}(f_{\rm esc} = 1)}. \quad (5)$$

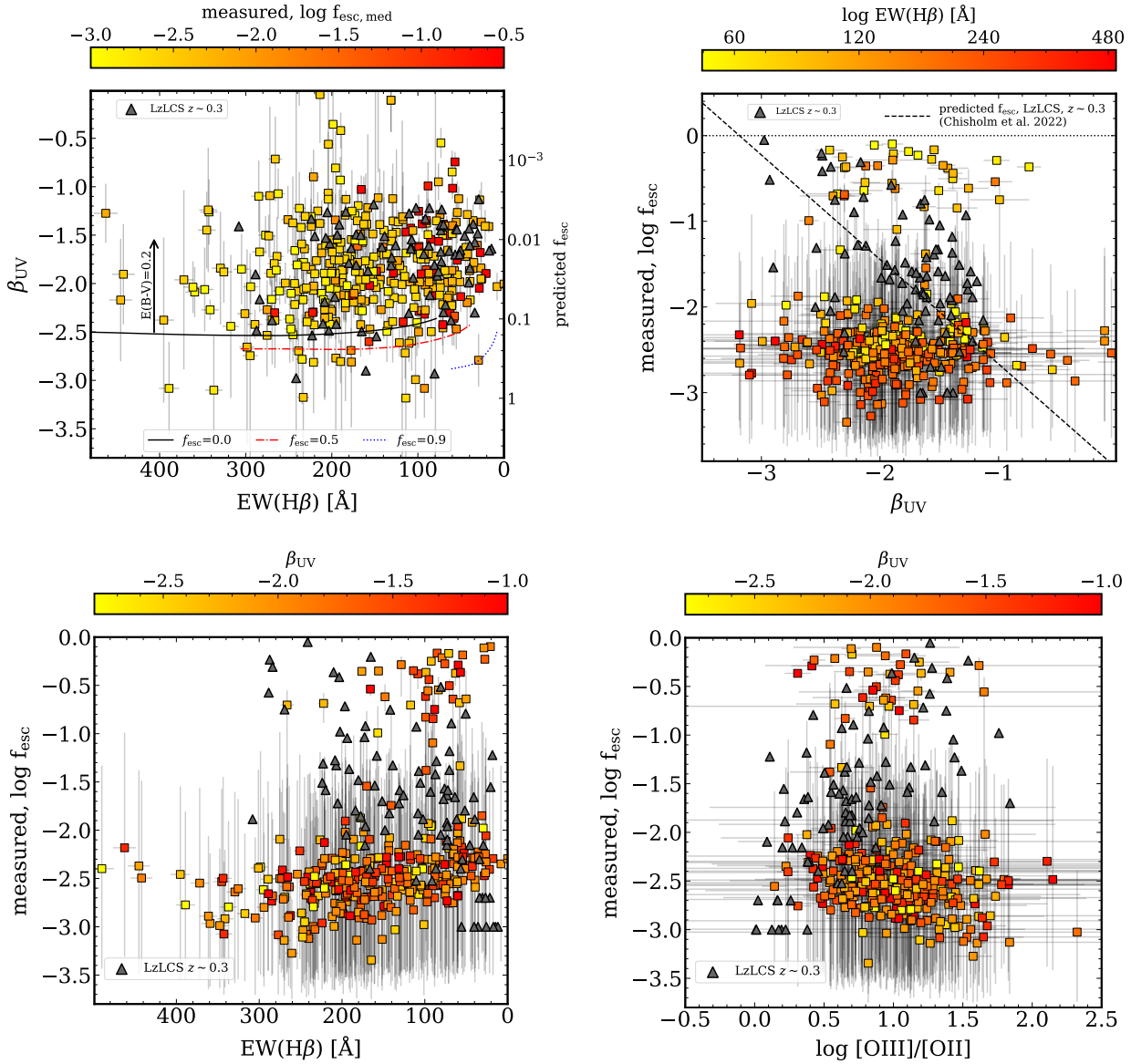


**Figure 11.** Relation between the UV spectral slope $\beta_{\rm UV}$, H$\beta$ EW, [O III]/[O II] ratio, and measured $f_{\rm esc}$ for galaxies in our sample. Each panel shows different projections of these quantities. The large data points show the samples here, and are color-coded as labeled. The triangles show measurements from LzLCS at $z \sim 0.3$ (S. R. Flury et al. 2022b). In the top-right panel, the right-hand axis shows the *predicted* $f_{\rm esc}$ using the UV spectral slope based on LzLCS from J. Chisholm et al. (2022). Unlike the prediction, there is no relation between the measured $f_{\rm esc}$ and UV spectral slope in our samples. In the top-left panel, the curves show the expected relation between $\beta_{\rm UV}$ and EW(H$\beta$) for a range of $f_{\rm esc}$ (as labeled). Each model assumes $Z = 0.05\ Z_{\odot}$ and a constant star formation history. These roughly bound the lower envelope of $\beta_{\rm UV}$ and EW(H$\beta$), where the arrow indicates the effects of dust attenuation with $E(B-V) = 0.2$.

This makes $\langle f_{\rm esc} \rangle$ the average weighted by the ionizing emissivity. We compute the result from Equation (5) for each iteration of the Monte Carlo simulation, and take the median as the quoted value with the 16th–84th percentile as the uncertainty. These values for $\langle f_{\rm esc} \rangle$ are listed in Table 6.

Figure 13 presents the Monte Carlo results for the volume-averaged $f_{\rm esc}$. The average inferred escape fractions show no evidence for evolution in redshift from $z \sim 5$ to 8, where the median values are $\langle f_{\rm esc} \rangle \simeq 3\%$–$7\%$. The 16th–84th percentile range varies slightly with redshift, but falls within $\simeq$1%–9%. This conclusion does not change appreciably if we integrate the UVLF to $M_{\rm UV} = -14$ mag (indicated by the short vertical red lines in Figure 13). This is because we have extended our relations to the fainter $M_{\rm UV}$ galaxies, assuming they follow the same distributions as those for galaxies at $M_{\rm UV} = -16$. However, if $M_{\rm UV} > -16$ galaxies have higher escape fractions, they will certainly increase the volume-averaged $f_{\rm esc}$ values (see, e.g., J. Y. C. Yeh et al. 2023).

The cosmic-averaged values of $f_{\rm esc}$ we derive at $4.5 < z < 9.0$ are consistent with measurements of the $f_{\rm esc}$ derived from galaxies at $z \sim$ 3–3.5 through direct measurements. These studies derive average $f_{\rm esc}$ by stacking spectroscopic or photometric data, and find $f_{\rm esc} \simeq 2\%$–$7\%$ (A. Grazian et al. 2017; C. C. Steidel et al. 2018; A. J. Pahl et al. 2021; R. Begley et al. 2022, and references therein) averaged over the population. Similar results were found by A. Saldana-Lopez et al. (2023) using relations between ISM absorption lines and other galaxy properties. While these are not directly comparable to the averages we derive (which are weighted by the UVLF), they provide additional evidence that the average $f_{\rm esc}$ at high redshift is relatively low.

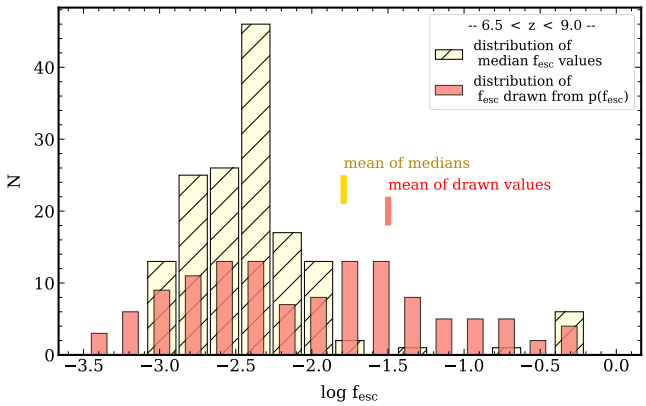


**Figure 12.** Distribution of the inferred LyC escape fraction, $f_{esc}$, for CEERS and JADES galaxies at $6.5 < z < 9.0$. The yellow hash-filled histogram shows the distribution of *median* values for each galaxy. These show that the mean $f_{esc}$ from the galaxy medians is $\simeq$1.5%. However, the red shaded histogram shows the distribution when we draw a random value from the $P(f_{esc})$ for each galaxy. In this case, the mean $f_{esc}$ is $\simeq$3%, roughly twice as high as for the mean of the *medians*, and there exists a small tail of objects with $f_{esc} \gtrsim 10\%$. This is a result of the $P(f_{esc})$ for most galaxies having a large tail extending to higher $f_{esc}$ (see Figure 7). We obtain similar results for galaxies at $4.5 < z < 6.5$.

**Table 6**
Inferred Volume-averaged Escape Fractions

| | $\langle f_{esc} \rangle$ | |
|---|---|---|
| $z$ | ($M_{UV} < -16$) | ($M_{UV} < -14$) |
| 5.0 | 0.065 ± 0.022 | 0.058 ± 0.024 |
| 6.0 | 0.055 ± 0.023 | 0.058 ± 0.026 |
| 7.0 | 0.027 ± 0.015 | 0.024 ± 0.024 |
| 8.0 | 0.026 ± 0.014 | 0.025 ± 0.017 |

Our finding of low average $f_{esc}$ runs contrary to most pre-JWST predictions, and predictions made using observations of local galaxies. B. E. Robertson et al. (2015, and references therein) argue that $f_{esc}$ needs to be 20% to achieve reionization at a redshift consistent with the CMB polarization. This is in part because these past studies assumed that EoR galaxies have relatively low ionizing production efficiencies, $\log \xi_{ion} = 25.2$, thus requiring higher $f_{esc}$ values. As we show below, high $f_{esc}$ values are unnecessary when the ionizing production efficiencies are high (see also J. B. Muñoz et al. 2024; C. Simmonds et al. 2024b). Interestingly, our results exceed the simulation-based $f_{esc}$ values from S. L. Finkelstein et al. (2019), who used these to match reionization timing constraints using variable $\xi_{ion}$ and $M_{lim}$ values. However, our results are consistent with predictions from the THESAN simulation for galaxies in our stellar mass range (J. Y. C. Yeh et al. 2023).

The volume-averaged values we derived would be much higher if we instead used $f_{esc}$ values based on correlations from LzLCS at $z \sim 0.3$. Figure 13 includes values for $\langle f_{esc} \rangle$ when we repeat the Monte Carlo simulation using correlations between $f_{esc}$ and $M_{UV}$ and the UV spectral slope ($\beta_{UV}$) predicted from LzLCS (J. Chisholm et al. 2019). In this case, the average $f_{esc}$ would be expected to increase with redshift over our redshift range, $4.5 < z < 9$, reaching $\langle f_{esc} \rangle > 0.1$ at $z \gtrsim 7$. This is strongly disfavored by our results, with significance exceeding $5\sigma$.

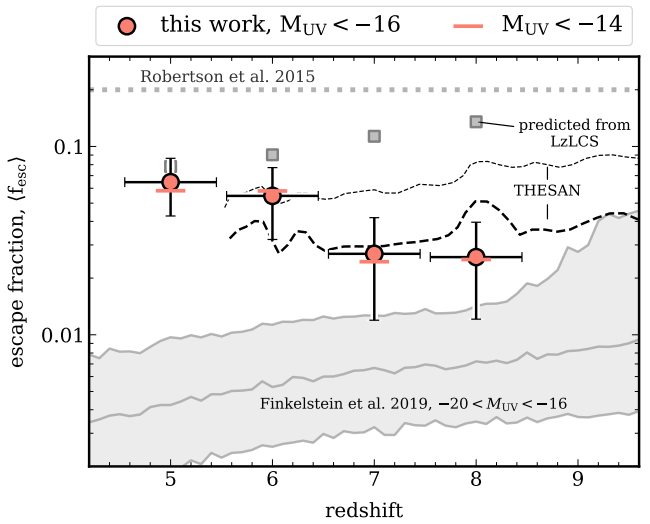


**Figure 13.** The volume-averaged inferred LyC escape fraction, $\langle f_{esc} \rangle$, for galaxies as a function of redshift. For each datum, we randomly select a value of $f_{esc}$ for each galaxy in the bin from its $P(f_{esc})$, and compute the volume-averaged value from Equation (5), integrating the UVLF to $M_{UV} < -16$. The error bars show the 16th–84th percentile range derived from the Monte Carlo simulation. The red horizontal dashes show the results if we integrate to $M_{UV} < -14$. The small gray boxes show the results assuming $f_{esc}$ values based on the relation from LzLCS at $z \sim 0.3$ (J. Chisholm et al. 2019). The dotted horizontal line shows the canonical value of $f_{esc} = 20\%$ (B. E. Robertson et al. 2015). The dashed lines show predictions from the THESAN simulation for the global galaxy population (light line) and galaxies with $\log M_*/M_\odot = 8 - 9$ (thick line; J. Y. C. Yeh et al. 2023). The shaded region shows simulation-based $f_{esc}$ values from S. L. Finkelstein et al. (2019), calculated to reproduce reionization using variable $\xi_{ion}$ and $M_{lim}$.

### 5.4. Challenges in Interpreting the Escape Fraction of EoR Galaxies

One challenge in interpreting our inferred $f_{esc}$ values is that they depend on the underlying stellar population models used in the SED fitting. The BPASS models used here have been demonstrated to reproduce the properties of young, metal-poor stellar populations dominated by short-lived massive stars under a variety of conditions (see, e.g., J. J. Eldridge & E. R. Stanway 2022), but it is conceivable that galaxies during the EoR host stellar populations with different properties (e.g., E. Zackrisson et al. 2011). Currently, some of the best evidence supporting the use of BPASS models comes from observations that these models reproduce the colors and emission-line properties of high-redshift galaxies (e.g., A. L. Strom et al. 2017; C. C. Steidel et al. 2018; G. M. Olivier et al. 2022; R. L. Larson et al. 2023). However, in some galaxies, photoionization models based on BPASS fail to reproduce extreme emission properties, including strong He II, C IV, [O III]/[O II], and other high-ionization emission lines (e.g., M. Lecroq et al. 2024). Several of these studies have invoked stellar populations that include stars with effective temperatures of $T_{eff} \sim$ 80–100 kK to explain the high-ionization emission lines and nebular continuum of galaxies (G. M. Olivier et al. 2022; A. J. Cameron et al. 2024; H. Katz et al. 2025). However, even if such conditions are present in our sample galaxies, they would *increase* the ionizing photon rate per unit UV luminosity, increasing $\xi_{ion}$. The existence of Population III stars or a top-heavy IMF would have a similar impact. If $\xi_{ion}$ is higher, matching the emission-line strengths would require increasing $f_{esc}$ to avoid overproducing the lines of the galaxies in our sample. That is, the product of $\xi_{ion} \times f_{esc}$

would increase, raising the cosmic ionization rate $\dot{n}_{\rm ion}$ and resulting in earlier reionization than indicated by CMB observations and IGM opacity studies of QSOs. This scenario therefore seems disfavored.

Another challenge is that the inferred escape fractions of galaxies at $4.5 < z < 9.0$ contrast strongly with expectations from scaling relations observed in low-redshift samples (e.g., LzLCS; S. R. Flury et al. 2022b). The H$\beta$ and [O III] emission-line EWs, [O III]/[O II] line ratios, and UV spectral slopes of the galaxies in our sample are similar in many ways to those in the LzLCS at $z \sim 0.3$. However, the escape fractions differ substantially (see Figure 11). Why this is the case is unclear. It may be that there are spatial disparities in the galaxies such that the regions with strong emission are physically distinct from regions with higher $f_{\rm esc}$, or that $f_{\rm esc}$ is not emitted isotropically such that the average $f_{\rm esc}$ is much lower when averaged over $4\pi$ steradians (see, e.g., C. L. Martin et al. 2024). This would impact direct measurements of the LyC emission, but not values such as ours that are inferred from the reprocessed nebular emission. Some studies of emission-line kinematics in $z \sim 0.3$ galaxies with LyC detections support this possibility, demonstrating that outflows can produce channels that promote higher $f_{\rm esc}$ (e.g., R. O. Amorín et al. 2024; S. R. Flury et al. 2025). Therefore, some of the key missing ingredients in interpreting the escape fractions may arise from variations in the spatial distribution of star formation, the gas-covering fractions, or both, all of which may differ substantially between low- and high-redshift galaxies.

Yet another challenge is that, theoretically, the escape fraction is difficult to calculate because it depends heavily on the connection between the effects of star formation and stellar feedback on the geometry, density, and ionization structure of the ISM (A. Ferrara & A. Loeb 2013; H. Xu et al. 2016). Radiation pressure and feedback from massive stars can create channels of ionized gas through which ionizing photons can escape, whereas other sight lines may be blocked by significant clumps of neutral gas that absorb the radiation (C. Clarke & M. S. Oey 2002). The escape fraction of each galaxy will have a temporal, radial, and angular dependence. In addition, many simulations may lack sufficient spatial resolution to resolve the details of the escape fraction on H II region scales (see, e.g., S. Mascia et al. 2024).

Nevertheless, theory provides some guidance, as many simulations predict low $f_{\rm esc}$ for galaxies with masses similar to those in our sample. Simulations generally predict that galaxies in the lowest-mass halos have the highest escape fractions, with $f_{\rm esc} \gtrsim 25\%$ (e.g., J. H. Wise et al. 2014; J.-P. Paardekooper et al. 2015; J. Y. C. Yeh et al. 2023; I. Kostyuk et al. 2025). However, these galaxies typically have $\log M_*/M_\odot < 7$, and are expected to contribute less than 10% of the total ionizing radiation (J. S. W. Lewis et al. 2020). Other work argues that there is a "peak mass" at which galaxies produce maximal $f_{\rm esc}$ (X. Ma et al. 2020). There may also be variations in dust production, as "attenuation-free models" favor $f_{\rm esc} < 10\%$ at $5 \lesssim z \lesssim 9$ (A. Ferrara et al. 2025). Many studies predict that higher-mass galaxies, $\log M_* \gtrsim 8$, like those in our sample, have $f_{\rm esc} \sim 1\%$–$5\%$ (H. Xu et al. 2016; J. Y. C. Yeh et al. 2023; I. Kostyuk et al. 2025), though other work finds higher values, $f_{\rm esc} \sim 5\%$–$15\%$ (H. Xu et al. 2016). This highlights that theoretical predictions have not yet converged, and underscores the importance of constraining the escape fraction empirically.

Simulations also predict a large variance in $f_{\rm esc}$ among galaxies. T. Kimm & R. Cen (2014) showed that galaxies may experience periods of high $f_{\rm esc}$, with a delay following a period of intense star formation. J. Rosdahl et al. (2018) used the SPHINX simulation to show that galaxies with high escape fractions, $f_{\rm esc} > 10\%$, occur only after a starburst, as feedback from the burst expels gas, temporarily halting star formation and increasing $f_{\rm esc}$ (see also K. S. S. Barrow et al. 2020; X. Ma et al. 2020; J. Rosdahl et al. 2022; H. Katz et al. 2023; I. Kostyuk et al. 2025). Therefore, it may be that the periods of highest specific SFR and $\xi_{\rm ion}$ production occur with low $f_{\rm esc}$, and vice versa, such that the product $f_{\rm esc}\xi_{\rm ion}$ is roughly constant (e.g., T. Kimm & R. Cen 2014). If this is the case, only a small fraction of galaxies would contribute to the leakage of LyC emission into the IGM at any given time (J.-P. Paardekooper et al. 2015). This scenario may also help explain the timing of reionization (e.g., S. L. Finkelstein et al. 2019, whose low volume-averaged $f_{\rm esc}$ values are illustrated in Figure 13), and the strong [O III]/[O II] emission in Ly$\alpha$-selected galaxies (A. Secunda et al. 2020; R. P. Naidu et al. 2022).

To summarize the challenges from theory, most cosmological simulations predict that $f_{\rm esc}$ is low in the majority of star-forming galaxies in the mass range of our sample, due to their high gas densities and the limited number of clear channels through which LyC radiation may escape. This is a very different physical situation to that observed in starburst galaxies at $z \sim 0.3$ with high LyC escape fractions, and may explain the differences between the observed properties and $f_{\rm esc}$ values in our sample (see Figure 11). This may be related to the fact that higher-redshift galaxies appear to have higher variance in their star formation histories (e.g., J. W. Cole et al. 2025), with theory predicting that the strong feedback associated with star formation can temporarily expel gas, pause star formation, and allow more LyC emission to escape (e.g., I. Kostyuk et al. 2025). The net effect is that the low values of $f_{\rm esc}$ we infer appear consistent with models, with important implications for reionization.

### 5.5. The Impact of High Ionizing Photon Production Efficiency and Low Escape Fraction on Reionization

The evolution of the cosmic ionizing rate density, $\dot{n}_{\rm ion}$, from Section 4.3 and Figure 9 allows us to estimate the evolution of the hydrogen-ionized fraction of the IGM, $x_e$. For each of Monte Carlo simulation, we solve the differential equation for this evolution. Following C. A. Mason et al. (2015, and references therein), we define

$$\dot{x}_e = \frac{\dot{n}_{\rm ion}}{\langle n_{\rm HI} \rangle} - \frac{x_e}{t_{\rm rec}}. \quad (6)$$

Here, $\langle n_{\rm HI} \rangle$ is the average IGM neutral hydrogen density, $\langle n_{\rm HI} \rangle = (1 - Q) n_{\rm H,0}$, where $n_{\rm H,0} = (1 - Y_p)(\Omega_{b,0}/m_p)\rho_{c,0}$ for a primordial helium mass fraction $Y_p = 0.2454$, baryon density parameter $\Omega_{b,0} = 0.049$, and critical density $\rho_{c,0}$, defined by $H_0 = 67.4$ km s$^{-1}$ Mpc$^{-3}$ (Planck Collaboration et al. 2020). The recombination time for H II is $t_{\rm rec}$, where we follow B. E. Robertson et al. (2015, and references therein) and take $t_{\rm rec} = [C\alpha_B(T) n_e (1 + z)^3]^{-1}$. The hydrogen recombination coefficient, $\alpha_B(T)$, depends on the temperature, for which we adopt the functional fit of L. Hui & N. Y. Gnedin (1997). The electron density is $n_e = (1 + Y_p/4X_p)\langle n_H \rangle$, where $X_p$ is the primordial hydrogen abundance. We further adopt the

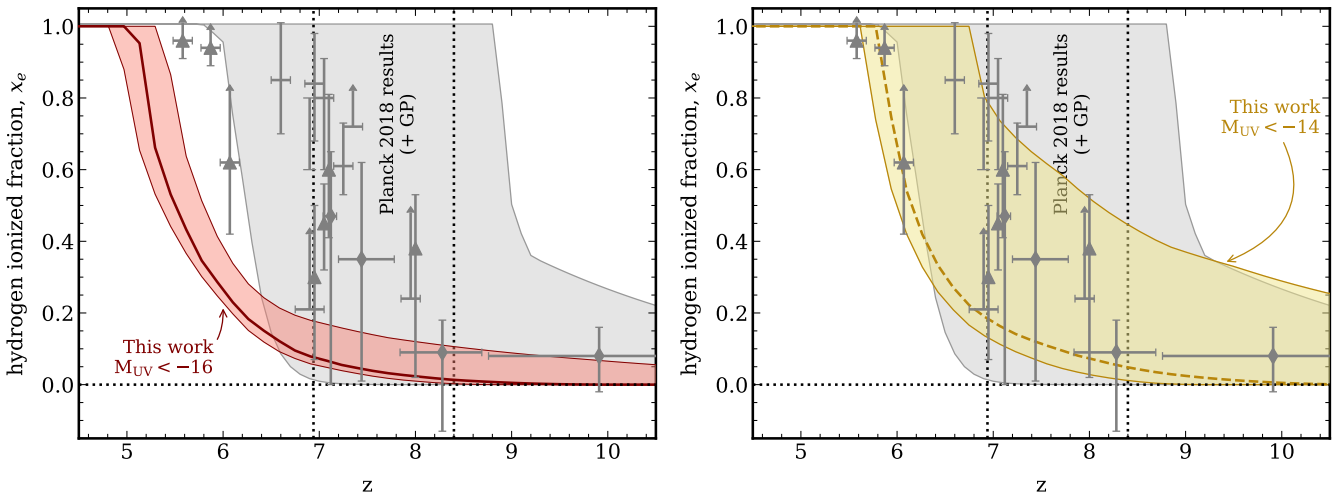


**Figure 14.** Evolution of the ionized fraction of the IGM, $x_e$. The curves and shaded regions show the results of our analysis based on integrating the UVLF to $M_{UV} < -16$ (left panel, red shaded region) and to $M_{UV} < -14$ (right panel, yellow shaded region). In each case, the width of the shading denotes the 16th–84th percentile range derived from the Monte Carlo simulation. In both panels the gray shaded region shows constraints from an analysis of Planck data with a prior using measurements of the Gunn–Peterson (GP) trough, where $x_e = 0.5$ corresponds to $z_{re} = 7.67 \pm 0.73$ (Planck Collaboration et al. 2020), indicated by the vertical dotted lines. The data points represent estimates based on the optical depth of absorbers in QSO sight lines, the evolution of Ly$\alpha$ emission in galaxies (I. D. McGreer et al. 2015; B. Greig et al. 2017; W. Hu et al. 2019; C. A. Mason et al. 2019; F. Wang et al. 2020; L. R. Whitler et al. 2020; H. Goto et al. 2021; M. Nakane et al. 2024), and measurements from damped Ly$\alpha$ profiles from the analysis of JWST spectra (H. Umeda et al. 2024). Our analysis favors a scenario where EoR galaxies produce sufficient ionizing photons to reionize the universe at times consistent with the CMB and QSO sight-line data.

evolution of the clumpiness factor, $C$, from the simulations of A. H. Pawlik et al. (2015), who find $C$ evolving from 4.8 at $z = 6$ to 1.5 at $z = 14$ (see also P. Madau et al. 1999; K. Finlator et al. 2011; S. L. Finkelstein et al. 2019; although see F. B. Davies et al. 2024, who argue for higher $C$ values). We then solve the differential equation (Equation (6)) for each iteration of the Monte Carlo simulation (Section 4.3) using the `ODEINT` routine in the `SciPy` package.

Figure 14 shows the evolution of the hydrogen-ionized fraction of the IGM, $x_e$, from our analysis. The thick solid line shows the median evolution from the Monte Carlo simulation, and the color-shaded regions show the 16th–84th percentile range of our results integrated to $M_{UV} < -16$ (left panel) and $M_{UV} < -14$ (right panel). For comparison, the gray shaded region in both panels shows the $1\sigma$ constraints on reionization from Planck CMB large-scale polarization measurements together with small-scale measurements of the kinematic Sunyaev–Zeldovich (kSZ) effect (S. Raghunathan et al. 2024) with a prior on $z_{end} = 6$ using measurements of the Gunn–Peterson (GP) trough (X. Fan et al. 2006). Excluding kSZ data (S. Raghunathan et al. 2024) reduces the constraining power on the high-$z$ end by a few percent. This shows that reionization is expected to begin by $z = 8.4$ and end shortly after $z = 7$ (vertical dotted lines; Planck Collaboration et al. 2020). Considering only galaxies brighter than $M_{UV} < -16$, we find that the hydrogen-ionized fraction reaches $x_e = 0.5$ at $z_{re} = 6.3$ (median), with a 68% confidence range of 5.3–5.8. Including fainter galaxies down to $M_{UV} < -14$, and again assuming $f_{esc}$ and $\xi_{ion}$ distributions similar to galaxies at $M_{UV} = -16$, we find that the hydrogen-ionized fraction of $x_e = 0.5$ is reached earlier, with a median $z_{re} = 7.7$ and range of 6.0–8.1 (68% confidence).

Our results provide evidence that galaxies in the EoR have high ionizing photon production efficiencies, $\xi_{ion}$, and low LyC escape fractions, $f_{esc}$. Combining these results with current UVLF constraints produces a cosmic photon ionization rate, $\dot{n}_{ion}$, sufficient to reionize the universe at times consistent with other observations. This averts the photon budget crisis (J. B. Muñoz et al. 2024), but only if our measurements reflect the $\xi_{ion}$ and $f_{esc}$ distributions of the full galaxy population. While we find low $f_{esc}$, this depends on the balance between the adopted stellar population synthesis models and the observed emission-line strengths. It is possible that JWST spectroscopic samples like ours are biased toward galaxies with strong nebular emission, which tend to have higher $\xi_{ion}$ and lower $f_{esc}$. As mentioned in Section 5.1, studies using photometric samples of galaxies, as well as some spectroscopic studies (A. Pahl et al. 2025), find a weaker relation between $M_{UV}$ and $\xi_{ion}$. If our sample is biased against galaxies with lower $\xi_{ion}$, particularly at faint UV magnitudes, the resulting cosmic ionizing rate density, $\dot{n}$, would be lower, leading to delayed reionization. Candidate galaxies for this case have been found in stellar-mass-limited photometric studies (C. Simmonds et al. 2024b). Confirming their $\xi_{ion}$ values and attempting to infer $f_{esc}$ will be paramount for understanding these biases. This will require deeper spectroscopy with JWST.

These results depend on several remaining uncertainties. One is the clumping factor, $C$, of the IGM, which we have assumed to be $C \simeq 2$–5 (see above). If $C$ is larger, as recently argued by F. B. Davies et al. (2024), a greater number of ionizing photons would be required to escape into the IGM at earlier times.

Another uncertainty is how fainter galaxies, $M_{UV} > -16$, impact reionization. This depends both on their properties and on the behavior of the UVLF, particularly the faint-end slope, and whether there is some minimum UV luminosity for galaxies in the EoR. Recent JWST studies have measured high $\xi_{ion}$ values for faint galaxies in the EoR (H. Atek et al. 2024; R. P. Naidu et al. 2024). However, it is unclear whether these galaxies constitute a biased subset for which emission lines are easiest to detect. Regarding the faint end of the UVLF, H. Atek et al. (2024) recently measured constraints from JWST, finding the steep slope extends to at least $M_{UV} = -13$. If such faint

galaxies are abundant and have high $\xi_{\rm ion}$, and especially elevated $f_{\rm esc}$, as predicted by models, they could contribute significantly to reionization, potentially reigniting the photon budget crisis (J. B. Muñoz et al. 2024). Regardless, we find that brighter galaxies $M_{\rm UV} < -16$ have $f_{\rm esc} \simeq 2\%$–$6\%$, which helps mitigate this crisis, and that fainter galaxies in the EoR with $M_{\rm UV} > -16$ must contribute for reionization to occur at times consistent with current constraints.

## 6. Conclusions

We have used new modeling of HST and JWST imaging and JWST/NIRSpec PRISM spectroscopic data to study the ionizing production efficiency and LyC escape fractions of galaxies at $4.5 < z < 9.0$. We use imaging and NIRSpec PRISM data for 412 galaxies from the CEERS and JADES surveys. We fit the data for each galaxy using BAGPIPES, simultaneously fitting stellar population and nebular emission components, with parameters to correct for slit losses and to account for the fraction of ionizing photons that escape the galaxy, $f_{\rm esc}$.

We measure the ionization production efficiency, $\xi_{\rm ion} = Q(H_0)/L_{\rm UV}$, using measurements of the Balmer emission-line strength taken from the NIRSpec data, combined with measures of the UV continuum luminosity from SED modeling (Section 4.1). In this way, the ionizing rate, $Q$, and UV luminosity, $L_{\rm UV}$, are derived from data with the same applied flux calibration. We find that the ionizing production efficiency increases with increasing redshift and decreasing UV luminosity. There is a scatter in the ionization production efficiency at fixed UV magnitude and redshift, $\sigma(\log \xi_{\rm ion}) \simeq 0.3$ dex. This means galaxies of fixed UV magnitude produce a range of ionizing photon rates.

We further constrain the ionizing photon escape fraction, which is driven by the strength of the nebular emission lines and the number of ionizing photons predicted from the stellar population models. For galaxies at $4.5 < z < 9.0$, the inferred escape fractions are typically low, with a median $f_{\rm esc} \lesssim 1\%$–$3\%$ (Section 4.2). We furthermore see no evidence for evolution in redshift or in $M_{\rm UV}$ over the range of our samples.

We use a Monte Carlo simulation to compute the cosmic ionizing rate density, $\dot{n}_{\rm ion}$ (Section 4.3). This simulation includes uncertainties in the UVLF, as well as our empirical distributions of $\xi_{\rm ion}$ and $f_{\rm esc}$. We find that, considering galaxies down to our observational limit, $M_{\rm UV} < -16$ mag, the cosmic ionizing rate density is $\log \dot{n} = 50.1 \pm 0.1$ at $z = 8$, rising to $50.5 \pm 0.1$ at $z = 5$. At redshifts $z > 6.5$, this is too low compared to the amount needed to reionize the universe as predicted by P. Madau et al. (1999). Extrapolating to fainter galaxies, $M_{\rm UV} < -14$ mag, increases the cosmic ionizing rate to $\log \dot{n} = 50.5 \pm 0.1$ at $z = 8$ and $\log \dot{n} = 50.7 \pm 0.1$ at $z = 5$, producing the required radiation for reionization by $z \sim 6$.

In our $4.5 < z < 9$ sample, the correlations between $\xi_{\rm ion}$ and galaxy properties are similar to those at lower redshifts, $1 < z < 3$ (Section 5.1). Galaxies with high $\xi_{\rm ion}$ exhibit larger EW(H$\beta$) and EW([O III]), as well as higher [O III]/[O II] ratios, implying that the elevated $\xi_{\rm ion}$ is associated with a relative increase in the number of O-type stars, and may reflect burstier star formation histories.

The correlations with $f_{\rm esc}$ in our $4.5 < z < 9$ sample differ from predictions based on correlations between $f_{\rm esc}$ and galaxy properties observed at $z \sim 0.3$ (Section 5.2). We find no correlation between the inferred $f_{\rm esc}$ and the UV spectral slope, $\beta_{\rm UV}$. We also find no strong correlations between $f_{\rm esc}$ and EW(H$\beta$), nor $f_{\rm esc}$ and [O III]/[O II]. This may be related to the different physical conditions in EoR galaxies compared to local starburst galaxies.

We also use our Monte Carlo simulation of the ionizing rate density to estimate the volume-averaged escape fraction, $\langle f_{\rm esc} \rangle$ (Section 5.3). For galaxies brighter than $M_{\rm UV} < -16$, we find $\langle f_{\rm esc} \rangle$ ranges from $3\% \pm 1\%$ at $z \sim 8$ to $7\% \pm 2\%$ at $z \sim 5$, with weak or no evolution over $4.5 < z < 9.0$. Including fainter galaxies, $M_{\rm UV} < -14$, results in only a small change, likely reflecting our assumption that galaxies with $M_{\rm UV} > -16$ share similar properties to those at $M_{\rm UV} = -16$. Our measurement of $\langle f_{\rm esc} \rangle$ contrasts strongly with pre-JWST inferences from $z \sim 0.3$ galaxies. However, our results are consistent with predictions from simulations (Section 5.4), where high gas column densities reduce $f_{\rm esc}$, except in cases where strong feedback from star formation expels the gas and clears channels through which LyC emission can escape. However, these events typically halt star formation, leading to lower $\xi_{\rm ion}$. Therefore, galaxies in the EoR may act to keep the product of $\xi_{\rm ion} \times f_{\rm esc}$ roughly the same. This will need to be tested using future datasets.

We estimate the impact of our measurements of $\xi_{\rm ion}$ and $f_{\rm esc}$ on reionization (Section 5.5) using the Monte Carlo simulation, and then solve for the evolution of the hydrogen-ionized fraction, $x_e$, as a function of redshift. Including galaxies brighter than $M_{\rm UV} < -16$ mag, the universe would not reach a hydrogen-ionized fraction of $x_e = 0.5$ until $5.3 < z < 5.8$ (68% confidence), consistent with the lower end of reionization based on QSO sight lines. Including an estimate of the contribution from fainter galaxies, $M_{\rm UV} < -14$ mag, reionization occurs sooner, with $x_e = 0.5$ obtained by $6.0 < z < 8.1$, broadly consistent with the CMB constraints. However, this assumes that galaxies with $-16 < M_{\rm UV} < -14$ have ionizing production efficiencies and escape fractions similar to galaxies with $M_{\rm UV} = -16$ mag. The implication is that, while EoR galaxies produce plenty of ionizing photons, this emission does not efficiently escape. We argue that this is a result of high gas fractions combined with bursty star formation histories, which together produce brief epochs during which galaxies have sufficiently clear gas channels to allow ionizing photons to escape.

Our results have several caveats. Among these is the assumption that we can constrain $f_{\rm esc}$ in galaxies through SED fitting. Our tests with simulated galaxy SEDs show that this is reasonable (Appendix B), but further validation will require extending the analysis to galaxies at lower redshifts with similar data and obtaining direct measurements of the LyC escape fractions. We plan to pursue this in a future study. Our results also depend on selection effects, where the samples may be biased toward objects with stronger nebular emission, favoring galaxies in a "burst" stage of star formation. However, even in this case, the implied $\xi_{\rm ion}$ values of galaxies in postburst stages would be lower, reducing the number of ionizing photons, unless these galaxies also have higher $f_{\rm esc}$. To test this will require more complete samples of galaxies in the EoR with JWST imaging and prism spectroscopy. This will become possible with forthcoming datasets that include larger samples of fainter galaxies (e.g., M. Dickinson et al. 2024).

## Acknowledgments

We wish to thank our colleagues in the CEERS collaboration for their hard work and valuable contributions on this project. We extend our sincerest thanks to the anonymous referee whose critical and constructive report improved the quality of this manuscript. We also thank the JADES team for providing an excellent dataset for science. We with to thank colleagues for valuable discussions, feedback, and suggestions, including John Chisholm, Kevin Huffenberger, Jessica Meh, Julian Muñoz, Irene Shivaei, Justin Spilker, Aaron Smith, and Romain Teyssier.

Portions of this research were conducted with the advanced computing resources provided by Texas A&M High Performance Research Computing (HPRC, http://hprc.tamu.edu).

This work benefited from support from the George P. and Cynthia Woods Mitchell Institute for Fundamental Physics and Astronomy at Texas A&M University. CP thanks Marsha and Ralph Schilling for generous support of this research. This work was partially support by the Future Investigators in NASA Earth and Space Science and Technology (FINESST) program grant No. 80NSSC23K1487. R.A. acknowledges support of grant PID2023-147386NB-I00 funded by MICIU/AEI/10.13039/501100011033 and by ERDF/EU, and the Severo Ochoa grant CEX2021-001131-S funded by MCIN/AEI/10.13039/50110001103. A.C.C. acknowledges support from a UKRI Frontier Research Guarantee Grant (PI Carnall; grant reference EP/Y037065/1) This work acknowledges support from the NASA/ESA/CSA James Webb Space Telescope through the Space Telescope Science Institute, which is operated by the Association of Universities for Research in Astronomy, Incorporated, under NASA contract NAS5-03127. Support for program JWST-ERS-01345.009-A, JWST-GO-02079.013-A, JWST-GO-06368.011-A, and JWST-GO-01837.030-A, was provided by NASA through a grant from the Space Telescope Science Institute, which is operated by the Association of Universities for Research in Astronomy, Inc., under NASA contract NAS 5-03127.

This work made use of v2.2 of the Binary Population and Spectral Synthesis (BPASS) models as described in E. R. Stanway & J. J. Eldridge (2018).

All the data used this work are available on MAST: JADES (M. Rieke et al. 2023, doi:10.17909/8tdj-8n28); CEERS (S. Finkelstein et al. 2023, doi:10.17909/z7p0-8481).

## Appendix A
## Comparison of Nebular Emission-line Fluxes from Models and Direct Measurements

In our SED fits, BAGPIPES models the nebular emission using the photoionization rate, $Q$, from the stellar populations, and converts it into a nebular spectrum. The nebular spectrum depends on the metallicity of the gas (taken to be equal to the metallicity of the stellar populations) and the ionization parameter, $U = n_\gamma/n_H$, the ratio of the density of ionizing photons to the gas density. The models assume a gas density $n_e = 100$ cm$^{-3}$, and that the models are "radiation bounded" such that all of the ionizing photons are absorbed by the gas and converted into nebular emission (A. C. Carnall et al. 2018). All of these assumptions are reasonable in the abstract, but may have deviations in practice.

One way to test the validity of the nebular models is to compare emission-line fluxes from the model fits to those measured directly from the spectra. We described our method to measure directly the emission-line fluxes in Section 3.3. We also repeated that process on the BAGPIPES model stellar populations that included the emission lines. Figure 15 compares these emission-line measurements for H$\alpha$, H$\beta$, [O III], and [O II]. The H$\alpha$ measurements are the most consistent in this comparison, with a median difference of 0.01 dex between the direct and model values, and a scatter (derived from the normalized absolute deviation) of 0.04 dex. Given that H$\alpha$ has a strong connection to the number of ionizing photons, it is encouraging that the models match the direct measures. The H$\beta$ emission is also very consistent, with a median difference of 0.0 dex and a scatter of 0.12 dex, consistent with the systematic uncertainty discussed in Section 3.4. The higher scatter for H$\beta$ compared to H$\alpha$ is driven in part by the fact that the line is weaker than H$\alpha$. However, there is also a population of galaxies for which the models favor higher H$\beta$ than observed directly. Many of these galaxies exhibit higher dust attenuation (all at $z < 6$), possibly indicating a departure from the assumed D. Calzetti (2001) dust attenuation law.

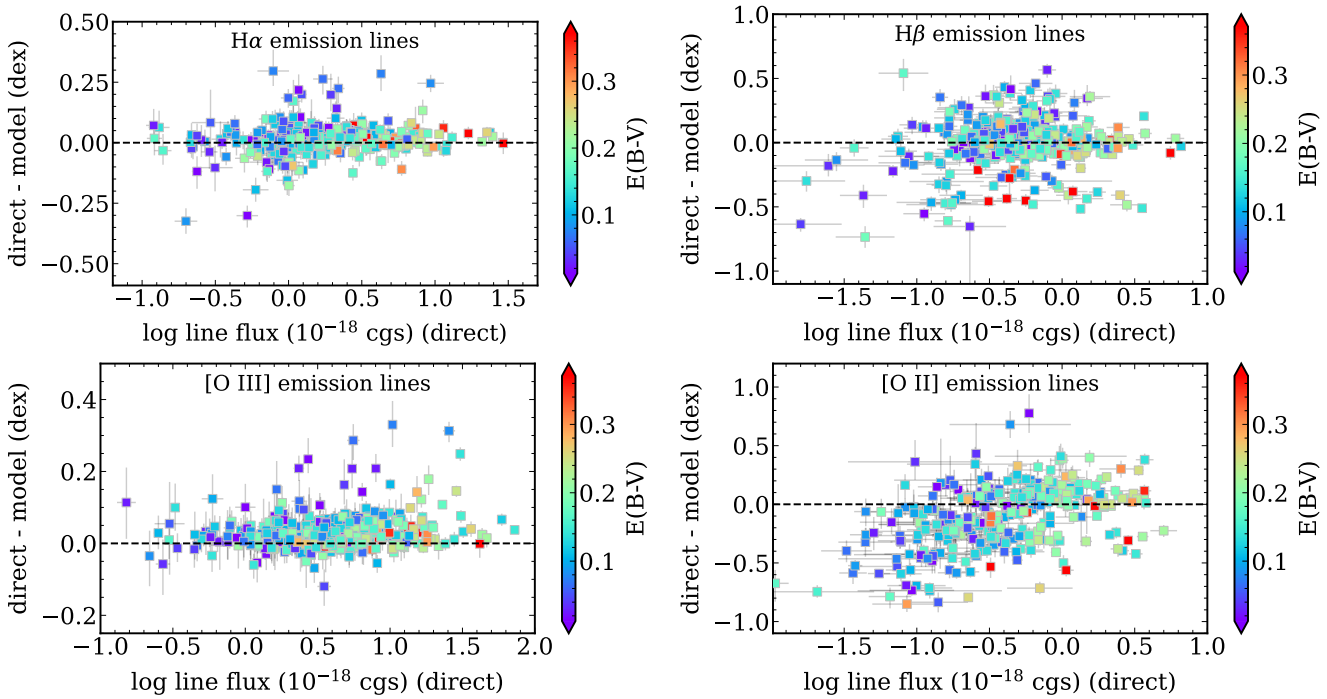


**Figure 15.** Comparison of emission-line fluxes for the sample of galaxies at $4.5 < z < 9.0$ considered here. Each panel shows the comparison for the strong nebular lines H$\alpha$, H$\beta$, [O III], and [O II], as labeled, in units of $10^{-18}$ erg s$^{-1}$ cm$^{-2}$. The abscissa in each panel shows the emission-line fluxes measured directly from the NIRSpec PRISM data for each galaxy, as described in Section 3.3. The ordinate in each panel shows the difference between the directly measured flux and the emission-line flux from the BAGPIPES models for each galaxy. The data points are color-coded by the median color excess derived from the SED modeling.

The comparison of the [O III] and [O II] emission lines is instructive. For [O III], the difference between the directly measured and modeled line fluxes is relatively small, with a median of 0.02 dex and a scatter of 0.03 dex. For [O II], however, there exists a much larger discrepancy, with a median of −0.08 dex and a scatter of 0.30 dex. This means that, *on average*, the [O II] emission predicted by the models is about 20% stronger than measured, though deviations can reach a factor of 2–3. There is no indication that this is caused by uncertainties in the dust modeling. Interestingly, the largest deviations occur for galaxies with *lower* overall measured [O II] emission. This may result from model assumptions regarding metallicity, density, temperature, and ionization parameter. Alternatively, it could indicate that the H II regions are density bounded, such that the [O II] regions of the nebula are not fully formed, as considered by C. Papovich et al. (2022, and references therein) to explain high [O III]/[O II] ratios in HST grism spectra of galaxies at $z \sim 1$–2. We plan to explore these aspects in a future study.

## Appendix B
## Measuring the Escape Fraction from SED Fitting

In this appendix, we assess the effectiveness of SED fitting in constraining $f_{\rm esc}$. We start with the SED model fit to galaxies in the CEERS sample. These include CEERS DDT 28 and 1518, depicted in Figures 2 and 8, as well as 30 other galaxies spanning the redshift range, $4.5 < z < 9.0$, and dust attenuation, $0.02 < A(V)/\mathrm{mag} < 1.0$, in the sample. These galaxies have relatively high S/Ns, which allows for relatively good constraints on their stellar population parameters. The sample includes galaxies at $z > 6.8$ and $z < 6.8$, for which the NIRSpec PRISM data respectively do and do not include H$\alpha$. For each galaxy, we take the best-fitting SED models and set $f_{\rm esc}$ to different values: $f_{\rm esc}$ = (0.005, 0.02, 0.05, 0.1, 0.2, 0.3, 0.5, 0.7). While we hold the other values fixed, the galaxies in this test span the full range of parameter space in $\log U$, $A(V)$, $Z/Z_{\odot}$, age, and star formation history; thus, the tests implicitly cover these parameters. Figure 16 presents examples of these models alongside the NIRSpec PRISM data for CEERS 1518 and DDT 28 in the region around H$\beta$ and [O III]. It is evident from the figure that as $f_{\rm esc}$ increases the strength of the nebular emission decreases, as expected.

We take the best-fit SED model for each galaxy and create a "mock" galaxy by simulating its NIRSpec PRISM spectrum and photometry in the CEERS JWST and HST bandpasses. We repeat this step, varying $f_{\rm esc}$. We then add noise to mimic a S/N = 10 for the photometric bands and a S/N = 3 for the spectrum in the region around H$\beta$ and [O III]. We then refit the data, deriving a posterior likelihood for $f_{\rm esc}$.

Figure 17 shows the results of this test. The panels on the left show examples of the simulated data and the best-fit models to those data for CEERS 1518 and DDT 28. The right panel compares the measured $f_{\rm esc}$ to the input values for all galaxies used here. Overall, there is good agreement, implying that the SED fitting can recover the $f_{\rm esc}$ values in this test. At high $f_{\rm esc}$, the agreement remains strong. At low values, $f_{\rm esc} \lesssim 0.03$, the fractional uncertainties increase, but the measured values still span the "true" values. This test is somewhat idealized as we are fitting the simulated data with the same suite of models used to create them. It will be important to compare the $f_{\rm esc}$ values derived from SED fitting, like those here, with $f_{\rm esc}$ values measured directly for galaxies with LyC observations, which we plan in a future study.

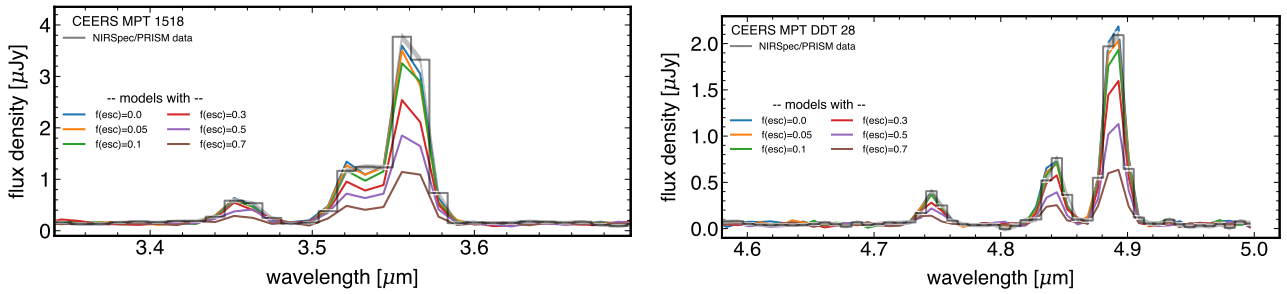


**Figure 16.** Example of varying $f_{esc}$ for two of the galaxies in our sample, CEERS 1518 and DDT 28. In each panel, the gray line and shading shows the NIRSpec PRISM data and uncertainties in the region around redshifted H$\beta$ and [O III]. The colored curves show a best-fit stellar population model, with $f_{esc}$ varied from 0.0 to 0.7 (as labeled). As $f_{esc}$ declines, the strength of the nebular emission drops as $(1 - f_{esc})$, which is evident in the relative strengths of the emission features.

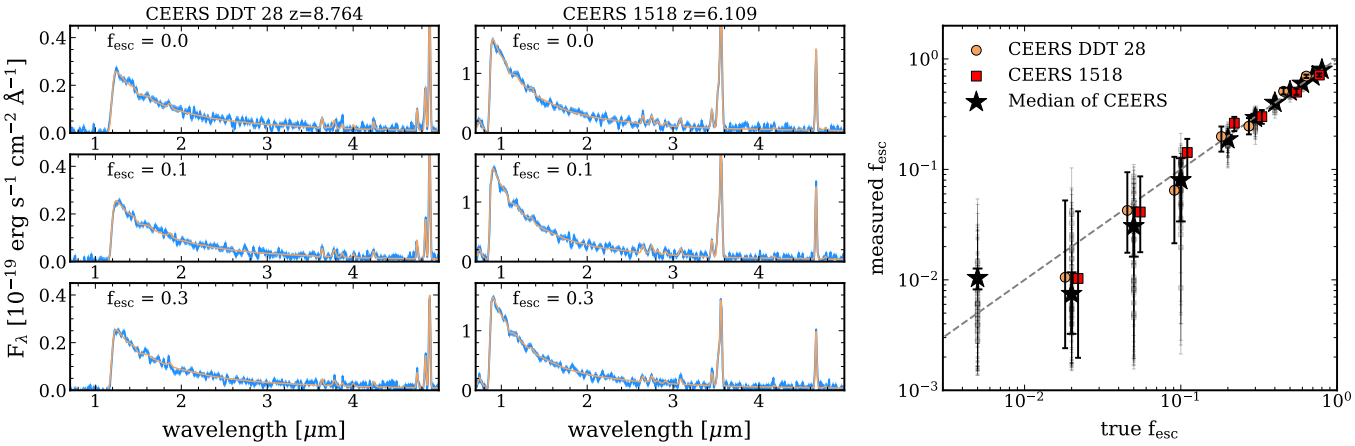


**Figure 17.** Results of fitting $f_{esc}$ for models with known input values. In the left and middle panels, the blue curves show the model spectra based on fits to two galaxies in our sample (CEERS DDT 28 at $z = 8.764$ and CEERS 1518 at $z = 6.109$), which are forced to have S/N $\approx 3$ in the region around the redshifted H$\beta$ and [O III] lines. The orange curves show the best-fit SED model. The right panel shows the recovered $f_{esc}$ values as a function of the (true) input values; values have been shifted slightly on the abscissa for clarity. The colored symbols show results for CEERS 1518 and DDT 28. The black stars show the median values for all galaxies in the CEERS sample used here. The error bars denote the 16th to 84th percentile range The recovered values trace well the input values, demonstrating the effectiveness of SED fitting in deriving $f_{esc}$ values. At high $f_{esc}$, the results show good agreement. At low values, $f_{esc} \lesssim 0.03$, the fractional uncertainties increase, but the measured values still span the "true" values.

## ORCID iDs

Casey Papovich https://orcid.org/0000-0001-7503-8482
Justin W. Cole https://orcid.org/0000-0002-6348-1900
Weida Hu https://orcid.org/0000-0003-3424-3230
Steven L. Finkelstein https://orcid.org/0000-0001-8519-1130
Lu Shen https://orcid.org/0000-0001-9495-7759
Pablo Arrabal Haro https://orcid.org/0000-0002-7959-8783
Ricardo O. Amorín https://orcid.org/0000-0001-5758-1000
Bren E. Backhaus https://orcid.org/0000-0001-8534-7502
Micaela B. Bagley https://orcid.org/0000-0002-9921-9218
Rachana Bhatawdekar https://orcid.org/0000-0003-0883-2226
Antonello Calabrò https://orcid.org/0000-0003-2536-1614
Adam C. Carnall https://orcid.org/0000-0002-1482-5818
Nikko J. Cleri https://orcid.org/0000-0001-7151-009X
Emanuele Daddi https://orcid.org/0000-0002-3331-9590
Mark Dickinson https://orcid.org/0000-0001-5414-5131
Norman A. Grogin https://orcid.org/0000-0001-9440-8872
Benne W. Holwerda https://orcid.org/0000-0002-4884-6756
Anne E. Jaskot https://orcid.org/0000-0002-6790-5125
Anton M. Koekemoer https://orcid.org/0000-0002-6610-2048
Mario Llerena https://orcid.org/0000-0003-1354-4296
Ray A. Lucas https://orcid.org/0000-0003-1581-7825
Sara Mascia https://orcid.org/0000-0002-9572-7813
Fabio Pacucci https://orcid.org/0000-0001-9879-7780
Laura Pentericci https://orcid.org/0000-0001-8940-6768
Pablo G. Pérez-González https://orcid.org/0000-0003-4528-5639
Nor Pirzkal https://orcid.org/0000-0003-3382-5941
Srinivasan Raghunathan https://orcid.org/0000-0003-1405-378X
Lise-Marie Seillé https://orcid.org/0000-0001-7755-4755
Rachel S. Somerville https://orcid.org/0000-0002-6748-6821
L. Y. Aaron Yung https://orcid.org/0000-0003-3466-035X

## References

Adams, N. J., Conselice, C. J., Austin, D., et al. 2024, ApJ, 965, 169
Amorín, R. O., Rodríguez-Henríquez, M., Fernández, V., et al. 2024, A&A, 682, L25
Arrabal Haro, P., Dickinson, M., Finkelstein, S. L., et al. 2023a, Natur, 622, 707
Arrabal Haro, P., Dickinson, M., Finkelstein, S. L., et al. 2023b, ApJL, 951, L22
Atek, H., Labbé, I., Furtak, L. J., et al. 2024, Natur, 626, 975
Bagley, M. B., Finkelstein, S. L., Koekemoer, A. M., et al. 2023, ApJL, 946, L12
Barrow, K. S. S., Robertson, B. E., Ellis, R. S., et al. 2020, ApJL, 902, L39
Becker, G. D., Pettini, M., Rafelski, M., et al. 2019, ApJ, 883, 163

Begley, R., Cullen, F., McLure, R. J., et al. 2022, MNRAS, 513, 3510
Begley, R., McLure, R. J., Cullen, F., et al. 2025, MNRAS, 537, 3245
Beverage, A. G., Kriek, M., Suess, K. A., et al. 2024, ApJ, 966, 234
Bhatawdekar, R., Conselice, C. J., Margalef-Bentabol, B., & Duncan, K. 2019, MNRAS, 486, 3805
Boutsia, K., Grazian, A., Giallongo, E., et al. 2011, ApJ, 736, 41
Bunker, A. J., Saxena, A., Cameron, A. J., et al. 2023, A&A, 677, A88
Calabrò, A., Castellano, M., Zavala, J. A., et al. 2024, ApJ, 975, 245
Calzetti, D. 2001, PASP, 113, 1449
Calzetti, D., Kinney, A. L., & Storchi-Bergmann, T. 1994, ApJ, 429, 582
Cameron, A. J., Katz, H., Witten, C., et al. 2024, MNRAS, 534, 523
Carnall, A. C., McLure, R. J., Dunlop, J. S., & Davé, R. 2018, MNRAS, 480, 4379
Carniani, S., Hainline, K., D'Eugenio, F., et al. 2024, Natur, 633, 318
Chabrier, G. 2003, PASP, 115, 763
Chisholm, J., Rigby, J. R., Bayliss, M., et al. 2019, ApJ, 882, 182
Chisholm, J., Saldana-Lopez, A., Flury, S., et al. 2022, MNRAS, 517, 5104
Choi, Y., Dalcanton, J. J., Williams, B. F., et al. 2020, ApJ, 902, 54
Choustikov, N., Katz, H., Saxena, A., et al. 2024, MNRAS, 529, 3751
Clarke, C., & Oey, M. S. 2002, MNRAS, 337, 1299
Cole, J. W., Papovich, C., Finkelstein, S. L., et al. 2025, ApJ, 979, 193
Cullen, F., McLure, R. J., McLeod, D. J., et al. 2023, MNRAS, 520, 14
Curti, M., D'Eugenio, F., Carniani, S., et al. 2023, MNRAS, 518, 425
Davies, F. B., Bosman, S. E. I., & Furlanetto, S. R. 2024, arXiv:2406.18186
D'Eugenio, F., Cameron, A. J., Scholtz, J., et al. 2025, ApJS, 277, 4
Dickinson, M., Amorin, R., Arrabal Haro, P., et al. 2024, JWST Proposal. Cycle 3, ID. #6368,
Dijkstra, M. 2014, PASA, 31, e040
Donnan, C. T., McLure, R. J., Dunlop, J. S., et al. 2024, MNRAS, 533, 3222
Eisenstein, D. J., Willott, C., Alberts, S., et al. 2023, arXiv:2306.02465
Eldridge, J. J., & Stanway, E. R. 2022, ARA&A, 60, 455
Endsley, R., Chisholm, J., Stark, D. P., Topping, M. W., & Whitler, L. 2025, ApJ, 987, 189
Faisst, A. L., Masters, D., Wang, Y., et al. 2018, ApJ, 855, 132
Fan, X., Carilli, C. L., & Keating, B. 2006, ARA&A, 44, 415
Fernández, V., Amorín, R., Firpo, V., & Morisset, C. 2024, A&A, 688, A69
Ferrara, A., Giavalisco, M., Pentericci, L., et al. 2025, OJAp, 8, 125
Ferrara, A., & Loeb, A. 2013, MNRAS, 431, 2826
Ferrara, A., Vallini, L., Pallottini, A., et al. 2019, MNRAS, 489, 1
Finkelstein, S., Bagley, M., & Yang, G. 2023, Data from The Cosmic Evolution Early Release Science Survey (CEERS) (STScI/MAST) doi:10.17909/Z7P0-8481
Finkelstein, S. L., Bagley, M., Song, M., et al. 2022, ApJ, 928, 52
Finkelstein, S. L., & Bagley, M. B. 2022, ApJ, 938, 25
Finkelstein, S. L., Bagley, M. B., Arrabal Haro, P., et al. 2025, ApJL, 983, L4
Finkelstein, S. L., D'Aloisio, A., Paardekooper, J.-P., et al. 2019, ApJ, 879, 36
Finkelstein, S. L., Leung, G. C. K., Bagley, M. B., et al. 2024, ApJL, 969, L2
Finlator, K., Oppenheimer, B. D., & Davé, R. 2011, MNRAS, 410, 1703
Flury, S. R., Jaskot, A. E., Ferguson, H. C., et al. 2022a, ApJS, 260, 1
Flury, S. R., Jaskot, A. E., Ferguson, H. C., et al. 2022b, ApJ, 930, 126
Flury, S. R., Jaskot, A. E., Saldana-Lopez, A., et al. 2025, ApJ, 985, 128
Giovinazzo, E., Oesch, P. A., Weibel, A., et al. 2025, arXiv:2507.01096
Goto, H., Shimasaku, K., Yamanaka, S., et al. 2021, ApJ, 923, 229
Grazian, A., Giallongo, E., Paris, D., et al. 2017, A&A, 602, A18
Greig, B., Mesinger, A., Haiman, Z., & Simcoe, R. A. 2017, MNRAS, 466, 4239
Grogin, N. A., Kocevski, D. D., Faber, S. M., et al. 2011, ApJS, 197, 35
Gunasekera, C. M., van Hoof, P. A. M., Dehghanian, M., et al. 2025, arXiv:2508.01102
Haardt, F., & Madau, P. 2012, ApJ, 746, 125
Hainline, K. N., Johnson, B. D., Robertson, B., et al. 2024, ApJ, 964, 71
Hayes, M. J., Saldana-Lopez, A., Citro, A., et al. 2025, ApJ, 982, 14
Heintz, K. E., Watson, D., Brammer, G., et al. 2024, Sci, 384, 890
Hu, W., Wang, J., Zheng, Z.-Y., et al. 2019, ApJ, 886, 90
Hui, L., & Gnedin, N. Y. 1997, MNRAS, 292, 27
Hutchison, T. A., Larson, R. L., Arrabal Haro, P., et al. 2024, JWST Proposal. Cycle 3, ID. #5507,
Inoue, A. K., Shimizu, I., Iwata, I., & Tanaka, M. 2014, MNRAS, 442, 1805
Iyer, K. G., Gawiser, E., Faber, S. M., et al. 2019, ApJ, 879, 116
Izotov, Y. I., Guseva, N. G., Fricke, K. J., et al. 2021, A&A, 646, A138
Izotov, Y. I., Schaerer, D., Thuan, T. X., et al. 2016, MNRAS, 461, 3683
Jaskot, A. E., Silveyra, A. C., Plantinga, A., et al. 2024, ApJ, 973, 111
Jung, I., Ferguson, H. C., Hayes, M. J., et al. 2024, ApJ, 971, 175
Juodžbalis, I., Maiolino, R., Baker, W. M., et al. 2026, MNRAS, in press
Katz, H., Cameron, A. J., Saxena, A., et al. 2025, OJAp, 8, 104
Katz, H., Saxena, A., Cameron, A. J., et al. 2023, MNRAS, 518, 592
Kelly, B. C. 2007, ApJ, 665, 1489
Khaire, V., & Srianand, R. 2015, MNRAS, 451, L30
Kimm, T., & Cen, R. 2014, ApJ, 788, 121
Kocevski, D. D., Finkelstein, S. L., Barro, G., et al. 2025, ApJ, 986, 126
Koekemoer, A. M., Faber, S. M., Ferguson, H. C., et al. 2011, ApJS, 197, 36
Kokorev, V., Chávez Ortiz, Ó. A., Taylor, A. J., et al. 2025, ApJ, 988, L10
Kostyuk, I., Ciardi, B., & Ferrara, A. 2025, A&A, 695, A32
Kreckel, K., Groves, B., Schinnerer, E., et al. 2013, ApJ, 771, 62
Lange, J. U. 2023, MNRAS, 525, 3181
Larson, R. L., Hutchison, T. A., Bagley, M., et al. 2023, ApJ, 958, 141
Lecroq, M., Charlot, S., Bressan, A., et al. 2024, MNRAS, 527, 9480
Leitherer, C., & Heckman, T. M. 1995, ApJS, 96, 9
Leja, J., Carnall, A. C., Johnson, B. D., Conroy, C., & Speagle, J. S. 2019, ApJ, 876, 3
Leung, G. C. K., Bagley, M. B., Finkelstein, S. L., et al. 2023, ApJL, 954, L46
Lewis, J. S. W., Ocvirk, P., Aubert, D., et al. 2020, MNRAS, 496, 4342
Livermore, R. C., Finkelstein, S. L., & Lotz, J. M. 2017, ApJ, 835, 113
Llerena, M., Pentericci, L., Napolitano, L., et al. 2025, A&A, 698, A302
Looser, T. J., D'Eugenio, F., Maiolino, R., et al. 2025, A&A, 697, A88
Looser, T. J., D'Eugenio, F., Maiolino, R., et al. 2024, Natur, 629, 53
Luo, B., Brandt, W. N., Xue, Y. Q., et al. 2017, ApJS, 228, 2
Ma, X., Kasen, D., Hopkins, P. F., et al. 2015, MNRAS, 453, 960
Ma, X., Quataert, E., Wetzel, A., et al. 2020, MNRAS, 498, 2001
Madau, P., Haardt, F., & Rees, M. J. 1999, ApJ, 514, 648
Martin, C. L., Peng, Z., & Li, Y. 2024, ApJ, 966, 190
Mascia, S., Pentericci, L., Calabrò, A., et al. 2024, A&A, 685, A3
Mason, C. A., Fontana, A., Treu, T., et al. 2019, MNRAS, 485, 3947
Mason, C. A., Trenti, M., & Treu, T. 2015, ApJ, 813, 21
Matthee, J., Sobral, D., Best, P., et al. 2017, MNRAS, 465, 3637
Maucherat-Joubert, M., Lequeux, J., & Rocca-Volmerange, B. 1980, A&A, 86, 299
McGreer, I. D., Mesinger, A., & D'Odorico, V. 2015, MNRAS, 447, 499
Méndez-Delgado, J. E., Skillman, E. D., Aver, E., et al. 2025, ApJ, 986, 74
Morales, A. M., Finkelstein, S. L., Leung, G. C. K., et al. 2024, ApJL, 964, L24
Muñoz, J. B., Mirocha, J., Chisholm, J., Furlanetto, S. R., & Mason, C. 2024, MNRAS, 535, L37
Naidu, R. P., Matthee, J., Kramarenko, I., et al. 2024, arXiv:2410.01874
Naidu, R. P., Oesch, P. A., van Dokkum, P., et al. 2022, ApJL, 940, L14
Nakajima, K., & Ouchi, M. 2014, MNRAS, 442, 900
Nakane, M., Ouchi, M., Nakajima, K., et al. 2024, ApJ, 967, 28
Nestor, D. B., Shapley, A. E., Kornei, K. A., Steidel, C. C., & Siana, B. 2013, ApJ, 765, 47
Ocvirk, P., Lewis, J. S. W., Gillet, N., et al. 2021, MNRAS, 507, 6108
Oey, M. S., & Kennicutt, R. C., Jr. 1997, MNRAS, 291, 827
Oke, J. B., & Gunn, J. E. 1983, ApJ, 266, 713
Olivier, G. M., Berg, D. A., Chisholm, J., et al. 2022, ApJ, 938, 16
Osterbrock, D. E. 1989, Astrophysics of Gaseous Nebulae and Active Galactic Nuclei (University Science Books)
Paardekooper, J.-P., Khochfar, S., & Dalla Vecchia, C. 2015, MNRAS, 451, 2544
Pahl, A., Topping, M. W., Shapley, A., et al. 2025, ApJ, 981, 134
Pahl, A. J., Shapley, A., Steidel, C. C., Chen, Y., & Reddy, N. A. 2021, MNRAS, 505, 2447
Pahl, A. J., Shapley, A., Steidel, C. C., et al. 2023, MNRAS, 521, 3247
Papovich, C., Cole, J. W., Yang, G., et al. 2023, ApJL, 949, L18
Papovich, C., Hu, W., Hutchison, T. A., et al. 2024, JWST Proposal. Cycle 3, ID. #5943,
Papovich, C., Simons, R. C., Estrada-Carpenter, V., et al. 2022, ApJ, 937, 22
Park, M., Conroy, C., Johnson, B. D., et al. 2025, ApJ, 994, 165
Pawlik, A. H., Schaye, J., & Dalla Vecchia, C. 2015, MNRAS, 451, 1586
Pérez-González, P. G., Costantin, L., Langeroodi, D., et al. 2023, ApJL, 951, L1
Planck Collaboration, Aghanim, N., Akrami, Y., et al. 2020, A&A, 641, A6
Plat, A., Charlot, S., Bruzual, G., et al. 2019, MNRAS, 490, 978
Prieto-Lyon, G., Strait, V., Mason, C. A., et al. 2023, A&A, 672, A186
Raghunathan, S., Ade, P. A. R., Anderson, A. J., et al. 2024, PhRvL, 133, 121004
Reddy, N. A., Kriek, M., Shapley, A. E., et al. 2015, ApJ, 806, 259
Rieke, M., Robertson, B., Tacchella, S., et al. 2023, Data from the JWST Advanced Deep Extragalactic Survey (JADES) (STScI/MAST) doi:10.17909/8TDJ-8N28
Robertson, B. E., Ellis, R. S., Furlanetto, S. R., & Dunlop, J. S. 2015, ApJL, 802, L19
Robertson, B. E., Tacchella, S., Johnson, B. D., et al. 2023, NatAs, 7, 611
Robertson, C., Holwerda, B. W., Young, J., et al. 2024, AJ, 167, 263

Rosdahl, J., Blaizot, J., Katz, H., et al. 2022, MNRAS, 515, 2386
Rosdahl, J., Katz, H., Blaizot, J., et al. 2018, MNRAS, 479, 994
Saldana-Lopez, A., Schaerer, D., Chisholm, J., et al. 2023, MNRAS, 522, 6295
Salmon, B., Papovich, C., Long, J., et al. 2016, ApJ, 827, 20
Sanders, R. L., Shapley, A. E., Jones, T., et al. 2021, ApJ, 914, 19
Saxena, A., Bunker, A. J., Jones, G. C., et al. 2024, A&A, 684, A84
Saxena, A., Pentericci, L., Ellis, R. S., et al. 2022, MNRAS, 511, 120
Scarlata, C., Hayes, M., Panagia, N., et al. 2024, arXiv:2404.09015
Scheuermann, F., Kreckel, K., Barnes, A. T., et al. 2023, MNRAS, 522, 2369
Secunda, A., Cen, R., Kimm, T., Götberg, Y., & de Mink, S. E. 2020, ApJ, 901, 72
Seillé, L. M., Buat, V., Fernández, V., et al. 2024, A&A, 689, A102
Shen, L., Papovich, C., Matharu, J., et al. 2025, ApJL, 980, L45
Shivaei, I., Reddy, N. A., Siana, B., et al. 2018, ApJ, 855, 42
Siana, B., Teplitz, H. I., Ferguson, H. C., et al. 2010, ApJ, 723, 241
Simmonds, C., Tacchella, S., Hainline, K., et al. 2024a, MNRAS, 527, 6139
Simmonds, C., Tacchella, S., Hainline, K., et al. 2024b, MNRAS, 535, 2998
Simons, R. C., Papovich, C., Momcheva, I. G., et al. 2023, ApJS, 266, 13
Stanway, E. R., & Eldridge, J. J. 2018, MNRAS, 479, 75
Steidel, C. C., Bogosavljević, M., Shapley, A. E., et al. 2018, ApJ, 869, 123
Strom, A. L., Steidel, C. C., Rudie, G. C., Trainor, R. F., & Pettini, M. 2018, ApJ, 868, 117
Strom, A. L., Steidel, C. C., Rudie, G. C., et al. 2017, ApJ, 836, 164
Tang, M., Stark, D. P., Chevallard, J., & Charlot, S. 2019, MNRAS, 489, 2572
Topping, M. W., Stark, D. P., Endsley, R., et al. 2022, ApJ, 941, 153
Trebitsch, M., Dayal, P., Chisholm, J., et al. 2022, arXiv:2212.06177
Trump, J. R., Arrabal Haro, P., Simons, R. C., et al. 2023, ApJ, 945, 35
Trussler, J. A. A., Conselice, C. J., Adams, N., et al. 2025, MNRAS, 537, 3662
Umeda, H., Ouchi, M., Nakajima, K., et al. 2024, ApJ, 971, 124
Vijayan, A. P., Yates, R. M., Lovell, C. C., et al. 2025, arXiv:2507.20190
Wang, F., Davies, F. B., Yang, J., et al. 2020, ApJ, 896, 23
Wang, X., Teplitz, H. I., Smith, B. M., et al. 2025, ApJ, 980, 74
Whitler, L. R., Mason, C. A., Ren, K., et al. 2020, MNRAS, 495, 3602
Williams, C. C., Tacchella, S., Maseda, M. V., et al. 2023, ApJS, 268, 64
Wise, J. H., Demchenko, V. G., Halicek, M. T., et al. 2014, MNRAS, 442, 2560
Xu, H., Wise, J. H., Norman, M. L., Ahn, K., & O'Shea, B. W. 2016, ApJ, 833, 84
Yang, G., Papovich, C., Bagley, M. B., et al. 2023, ApJL, 956, L12
Yeh, J. Y. C., Smith, A., Kannan, R., et al. 2023, MNRAS, 520, 2757
Yung, L. Y. A., Somerville, R. S., Finkelstein, S. L., et al. 2020a, MNRAS, 496, 4574
Yung, L. Y. A., Somerville, R. S., Popping, G., & Finkelstein, S. L. 2020b, MNRAS, 494, 1002
Zackrisson, E., Rydberg, C.-E., Schaerer, D., Östlin, G., & Tuli, M. 2011, ApJ, 740, 13